

JET-P(92)29

M.G. von Hellermann, H.P. Summers
and JET Team

Atomic Modelling and Spectroscopic Diagnostics

“This document contains JET information in a form not yet suitable for publication. The report has been prepared primarily for discussion and information within the JET Project and the Associations. It must not be quoted in publications or in Abstract Journals. External distribution requires approval from the Publications Officer, JET Joint Undertaking, Abingdon, Oxon, OX14 3EA, UK”.

“Enquiries about Copyright and reproduction should be addressed to the Publications Officer, EFDA, Culham Science Centre, Abingdon, Oxon, OX14 3DB, UK.”

The contents of this preprint and all other JET EFDA Preprints and Conference Papers are available to view online free at www.iop.org/Jet. This site has full search facilities and e-mail alert options. The diagrams contained within the PDFs on this site are hyperlinked from the year 1996 onwards.

Atomic Modelling and Spectroscopic Diagnostics

M.G. von Hellermann, H.P. Summers
and JET Team*

JET-Joint Undertaking, Culham Science Centre, OX14 3DB, Abingdon, UK

** See Annex*

Preprint of Paper to be submitted for publication in
Review of Scientific Instruments

ATOMIC MODELLING AND SPECTROSCOPIC DIAGNOSTICS

M. G. von Hellermann and H. P. Summers

JET Joint Undertaking, Abingdon, Oxon., OX14 3EA, U.K.

Atomic reaction models provide the link by which quantitative diagnostic comments on plasma behaviour and parameters may be made from spectral observations of emission by ions in the plasma. The paper reviews progress in this area with emphasis on impurity species in magnetic confinement fusion plasmas. A systematic approach based on generalised collisional-radiative theory is adopted and items discussed include spectroscopy of edge and divertor environments, beam emission and charge exchange spectroscopy. Case studies are based on experience at the JET Joint European Torus Experiment.

I. OVERVIEW

In general, atomic modelling forms one part of an analysis system in spectroscopic diagnostic application. Analysis systems, though differing in detail, have points of similarity whatever the plasma or particular spectroscopic instrumentation under study. If the atomic modelling aspect is approached with care, it can be organised in a manner of fairly universal usefulness and

usability. We outline issues which a general atomic modelling system must address and how we have handled this at the Joint European Torus Experiment (JET). The paper then becomes more specific to fusion plasmas and examines the links to fusion plasma models and zones of interest. The latter include the plasma edge, divertors, beam penetrated plasma and the near equilibrium core plasma. The special aspects of the atomic modelling required to support these areas in JET are described. Finally, we give case studies to demonstrate the 'philosophy' of our approach.

The analysis viewpoint is shown schematically in fig.1. An implicit assumption is that the separability of the different parts can take place. For the atomic modelling / plasma modelling distinction, the separation is based on timescales.

A. Populations and timescales

Consider the various states of an ion and its population densities in a plasma. The lifetimes of different types of state vary enormously. We can for example identify resonant states, such as occur in dielectronic recombination, of very short (Auger) lifetimes; bound excited states, which can freely cascade, of short (radiative) lifetimes; ground and metastable states of ions with relatively long (ionisation, recombination or forbidden decay) lifetimes. It is convenient to treat ground and metastable states under the single classification 'metastables'. The relaxation times of the various populations in a plasma therefore satisfy an inequality of the form

$$\tau_{\text{autoionising state}} \ll \tau_{\text{excited state}} \ll \tau_{\text{metastable state}}$$

More precisely, consider the states of the z -times ionised ion X^{+z} of an element X . Then with considerable simplification $\tau_{as} \simeq 10^{-12}$ sec, $\tau_{es} \simeq 10^{-7}/z^4$ sec and $\tau_{ms} \simeq 10^8 z^3/N_e$ sec with N_e the electron density. In any plasma, the distances particles move in their lifetime compared with plasma scale lengths or their lifetimes compared with the timescales of gross plasma change divide the populations naturally into 'quasi-static populations', which relax rapidly compared with plasma timescales and therefore satisfy a local equilibrium, and 'dynamical populations', which relax on comparable or slower timescales than the plasma and require solution of coupled, time dependent transport equations. The latter of course constitute a plasma model. For laboratory fusion plasma and many astrophysical plasmas, resonant states and excited states belong to the first category and metastables to the second. It follows that only the metastable states have large populations in the fusion plasma. Atomic modelling can, as an isolated task, (a) provide solutions for excited populations as functions evaluated at local conditions in equilibrium which multiply instantaneous metastable populations; (b) provide effective rates evaluated at local conditions connecting metastable populations within and between ionisation stages which are the source terms of the plasma model equations.

B. Collisional-radiative equations

As is well known, collisional-radiative theory gives the necessary connections. The formal relationships have been written down on a number of occasions ¹. The complexity of the 'collisional radiative' rates is because they include indirect (sometimes called stepwise and redistributive) processes. In most work at low density, such processes with the exception of simple radiative cascade are ignored, giving the so-called 'coronal approximation'. Also metastable states are ignored, each ionisation stage being assumed to have only a single 'ground' state. Unfortunately, at the higher density and lower temperature environments of current interest, these simplifications are incorrect and the full collisional-radiative picture must be used. The collisional radiative picture is very general with various primary collision processes influencing the populations, such as electron impact excitation, charge exchange recombination from neutral hydrogen in beams and so on. Once the primary processes are identified, the associated densities, such as N_e , N_H are usually factored out leaving the more familiar collisional-radiative coefficients.

The emissivity and line of sight integrated emission of any spectrum line in terms of the metastable populations follows immediately. For simplicity suppose the z -times ionised atom X^{+z} has only a ground state g and a metastable state m , and that the next ionisation stage $z + 1$ has a single ground state g' . Also suppose electron excitation, free electron capture and charge exchange recombination from neutral hydrogen are the dominant processes. The line of sight emission in the transition $i \rightarrow j$ in the ion of charge z may be written as

$$\begin{aligned}
I(i \rightarrow j) &= \int A(i \rightarrow j) N_i^{(z)} dl \\
&= \int q_{eff.}^{ex.}(i \rightarrow j; g) N_e N_g^{(z)} dl + \int q_{eff.}^{ex.}(i \rightarrow j; m) N_e N_m^{(z)} dl \\
&+ \int q_{eff.}^{rec.}(i \rightarrow j; g') N_e N_{g'}^{(z+1)} dl + \int q_{eff.}^{cx.}(i \rightarrow j; g') N_H N_{g'}^{(z+1)} dl
\end{aligned} \tag{1}$$

where the N denote population densities. The first part in each integral is the so called 'effective emission coefficient' and the last density product integral is the associated 'emission measure'.

In this case the effective coefficients connecting the ground and metastable states are usually written as 'collisional radiative ionisation coefficients' $S_{CR}(z, g \rightarrow z + 1, g')$ and $S_{CR}(z, m \rightarrow z + 1, g')$; 'collisional radiative recombination coefficients' $\alpha_{CR}(z + 1, g \rightarrow z, g)$ and $\alpha_{CR}(z + 1, g \rightarrow z, m)$; 'collisional radiative cross coupling coefficients' $q_{CR}(z, m \rightarrow z, g)$. The theoretical calculation of all these effective coefficients is the atomic modelling task.

II. PLASMA MODELS AND EMISSION

A. Plasma models

It is not intended to discuss plasma models in detail here. Evidently these are legion and specific. There are however four models of general interest.

The *coronal ionisation equilibrium model* applies well to highly ionised species in the low density solar atmosphere and fairly well to very highly ionised

heavier species in the core of fusion plasmas. Electron impact is assumed to be the cause of transitions, only the ground state of each ionisation stage is assumed significantly populated and ionisation timescales are short compared with plasma timescales. Ionisation equilibrium has time to be established locally so

$$\{N_g^{(z+1)}/N_g^{(z)}\}_{equil.} = q_{eff}(z,g \rightarrow z+1,g)/\alpha_{eff}(z+1,g \rightarrow z,g) \quad (2)$$

Only the first integral in equation (1) contributes and it is reorganised in the solar case as

$$I(i \rightarrow j) = \{N_X^{tot}/N_H\} \int q_{eff}^{ex.}(i \rightarrow j; g) \{N_g^{(z)}/N_X^{tot}\} \{N_H/N_e\} N_e^2 dl \quad (3)$$

The first part of the integrand with the equilibrium assumption (2) is called the $g(T_e)$ function for the line and the second part is rewritten as

$$N_e^2 dl = \{N_e^2 dl/dT_e\} dT_e \quad (4)$$

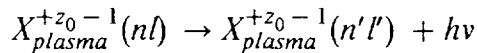
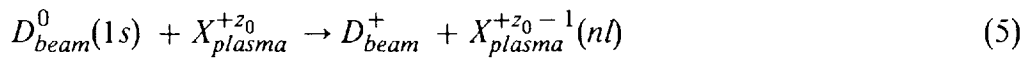
with the part in $\{\}$ brackets called the differential emission measure. Note the $g(T_e)$ function depends also on density and here includes the electron to hydrogen density ratio. The constancy of the relative cosmological element abundance is assumed. In fusion application the assumptions and inclusions in the $g(T_e)$ function are modified and the emission measure redefined appropriately. Solar astrophysicists measure many lines of different elements in different ionisation stages and using calculated $g(T_e)$'s seek to invert the

integral to obtain the differential emission measure. The different lines probe different temperature regions of the atmosphere. The more completely they do this the better the integral inversion can be done (see fig.2) ². By contrast, in the fusion case, the electron temperature and electron density spatial variations are often known from independent measurement. The calculated emission is used to seek the impurity abundance. A further interesting development may occur in fusion plasmas at very low temperatures when a substantial neutral hydrogen presence alters the local ionisation balance through an extra charge transfer contribution to the recombination coefficients. Considering only this effect, the total equilibrium radiated power for beryllium is shown in fig.3. At $10eV$, the dominant ionisation stage is Be^{+2} . However the temperature is too low to excite its spectrum. Be^{+1} , though very much lower in fractional abundance, is the primary radiator. Charge exchange influences strongly this small fraction and therefore has an inordinate effect on the radiated power.

The *extreme ionising model* applies to neutral and near neutral species entering a high temperature plasma from a boundary surface such as a limiter or divertor target plate. The species ionises rapidly through several ionisation stages while still near the surface from which it was born. Recombination at least for the low ionisation stages may be ignored. For sufficiently low neutral hydrogen densities, electron collisions are the driving reactions. In these circumstances the metastable states are far from a quasistatic balance. A time dependent model (or spatial model if a fixed inflowing speed is assumed) for the metastables is essential. A simple solution may be obtained

if a ground state neutral is assumed suddenly placed in a plasma of fixed electron temperature (T_e). The collisional radiative ionisation and cross coupling coefficients required for such a calculation for neutral beryllium are shown in fig.4a. Be^0 has a ground state $2s^2\ ^1S$ and metastable state $2s2p\ ^3P$. The ratio of the time integrated populations of these is much smaller than the ratio which would occur in equilibrium at T_e (fig.4b). Neutral beryllium, born in it's ground state and flowing into a high temperature plasma has an underabundant metastable population (see ³ for details). The use of calculated 'photon efficiencies' in deducing fluxes is important and well established ^{4,6}.

The *charge exchange spectroscopy (CXS) model* activated by neutral beams (such as fast high energy neutral deuterium or helium heating beams in JET) provides a marked contrast. The primary reactions leading to emission are state selective capture into excited states of fully ionised impurities followed by radiative decay.



Usually redistributive collisions intervene to alter the l -distribution of the populations before the radiative decay. Only the last term in equation 1 contributes to the observed emission. The emission measure is $\int N_D^{beam} N_{z_0} dl$. Since emission is localised at the beam/plasma/viewing line intersection (short $\int dl$) with nearly constant conditions, the effective emission may be

taken outside the integral. Extensive collisional radiative data of q_{eff} for fully stripped light ions in the visible and UV spectral range are available^{5,6,7}.

Beam emission spectroscopy (BES), in which the neutral beam atoms themselves are excited by the background plasma and then radiate, is closely related⁹. The primary reactions are collisional excitation of the beam atoms by electrons, deuterons and fully stripped ions in the plasma. The plasma model is that of the beam attenuation to the observed volume and is necessary to resolve the emission measures into separate densities. The effective ionisation coefficients for the model consist at low density, of the direct losses from the beam atoms in their ground state. For D^0 beams it is given by the sum of the reactions (5) and the direct ionising reactions by plasma electron and ions. At higher densities, the stepwise processes as given by the full collisional radiative coefficient is required. Fig.5 compares neutral deuterium densities in the JET heating beams as calculated from the attenuation model and as deduced from the observed D_{α} emission at several viewing lines intersecting the beams. It constitutes a strong test of atomic modelling and plasma modelling.

Other plasma models used in fusion are more specific in geometry and boundary conditions and use independent (non-spectroscopic) measurements as part of their input data. Of special interest at this time are 1-D radial impurity diffusive transport models, 1-D and 2-D scrape-off-layer and divertor fluid models, Monte Carlo neutral and impurity diffusion models. The main point at issue for this paper is that necessary atomic data is made available and flows easily into these models in the same way as in the general examples above.

B. Spectral features

In the diagnostic loop some thought must be given to the assembly of predicted features and the disassembly of observed features. Theoretically as we proceed down the diagnostic loop, we advance from *feature primitives* associated with a particular excited state (or a bundle of excited states) to *features* in which primitives are related to the metastables to *superfeatures* in which features at different times or positions are combined according to lines of sight and spectrometer characteristics⁸. It is the latter which are compared with observation.

C. The atomic data and analysis structure

Evidently collisional-radiative modelling upon which the approach of this paper is based, requires substantial fundamental atomic rate coefficient data and procedures for its conversion to the derived coefficients of the type described above used in practise. At JET we take a unified approach to this called 'The Atomic Data and Analysis Structure', ADAS. ADAS is an interactive system composed of a fundamental atomic database, collisional-radiative processing codes, and a derived database. The latter can be accessed by experiment analysis codes. The fundamental database is in part constructed around *specific ion files* each of which can support directly a population calculation. These are created both semi-automatically (for example using multielectron-multiconfiguration structure and distorted wave collision codes) and in detailed targetted assessments. Special attention is given to isoelectronic sequence interpolation and extrapolation through the assembly

of *general z files*. These allow automatic creation of an intermediate ion specific z file where no specific data is available. ADAS has extensive data on ion/atom collision cross-section data including state selective charge transfer. These support a large diagnostic effort on charge exchange and beam emission spectroscopy. Derived data in ADAS includes comprehensive collisional-radiative ionisation and recombination data, radiated power etc., effective emission coefficients (both electron driven and charge exchange driven), photon efficiencies, finite density beam attenuation coefficients etc. Interactive database interrogation and extraction is supported as well as specific calculations for database extension, population studies and diagnostic line ratio investigations, derived database updating and preparation of private data collections.

III. CASE STUDIES

A. Superfeatures and the observed spectrum disassembly

Central plasma data can be deduced from line of sight measurement of the Doppler width and shift of the resonance line of helium-like Nickel, especially the ion temperature and toroidal velocity (see ¹⁰ for the detailed study). In the case of the JET geometry, the line of sight of the high resolution x-ray spectrometer covers a range of significantly changing plasma input data ($N_e, T_e, v_{toroidal}$) which leads to a spectrum resulting from an integration over several emission layers. The radial emission profile of the Ni resonance line

is calculated from the fusion plasma variant of the $g(T_e)$ function using measured electron temperature and density profiles. The modelled 'superfeature' is fitted to the observed spectrum and central temperatures and velocities extracted. A comparison of untreated line-of-sight averaged data and modelled central data with independent CXRS shows the the importance of the profile superpositions and the final excellent agreement ¹⁰.

Atomic and plasma modelling of charge capture and beam stopping processes and consistency checks with independent plasma data (Z_{eff} , N_e , and thermal neutron emissivity) require an assessment of all relevant plasma ions. At the JET tokamak central densities of C , Be and He and radial profiles of either C or Be are simultaneously monitored together with beam emission spectroscopy of either DI or HeI. One of the most complex examples of a combined modelling effort on the prediction of 'cold' (10eV to 1000 eV) plasma boundary features and 'hot' (0.5 keV to 30 keV) charge exchange core features is the spectral range at $4686 \text{ \AA} \pm 100 \text{ \AA}$ for the combined HeII and BeIV spectrum (fig.6) ^{9,11}. The wavelength coincidence with the HeII CX line ($n = 4-3$ at 4685.25 \AA) requires a coupled-fit technique for the simultaneous extraction of HeII and BeIV CX photon fluxes. Modelling of charge capture cross-sections and experimental data have given a ratio $(n = 6-5)/(n = 8-6) = 5.3$ for the BeIV CX emission ⁶ The spectrum was observed during a 135 keV 3He neutral beam fuelling JET pulse. The broad pedestal with a halfwidth of $\Delta\lambda = \lambda_0 \times v_{beam}/c = 45 \text{ \AA}$ is attributed to the CX reaction between slowing-down He^{+2} particles and the neutral He^0 beam. It is at a clearly enhanced level above bremsstrahlung which is typically some

10^9 photons/cm²sec.sr.Å. In practise, logarithmic mapping of log(I) versus energy of the combined core CX and boundary emission spectrum of HeII shows most clearly the slowing-down features of injected helium. The charge exchange effective emission coefficient q_{eff}^{cx} of HeII(n=4-3) for a neutral helium beam acting as a donor is used for the calculation of the spectrum produced by slowing-down alphas ^{7,8}. The input distribution function is an anisotropic Fokker-Planck calculation for the slowing-down velocity distribution function for neutral beam injection ¹². The effective emission coefficient derived by the simulation enables the deduction of fast particle densities. Further results correlating observed fast particle densities and the temporal evolution of thermalised alpha particle population with neutral beam powers will be described in a future paper.

B. Consistency of impurity deduction and neutral beam stopping

The calculation of neutral beam stopping processes in a fusion plasma shows that the stopping cross-sections have a non linear Z dependence (fig.7) This implies that for a consistent treatment of a charge exchange analysis all plasma ion constituents need to be known. The difference in beam attenuation for a pure hydrogen or a pure impurity plasma is substantial (fig. 7b). For the deduction of impurity densities from measured CXRS photon fluxes a local neutral beam strength is required. This can be either calculated from external data such as electron density and Z_{eff} or alternatively deduced from beam emission spectroscopy (fig. 5). An accurate beam stopping calculation however needs as input the densities of impurity ions. The iterative problem

can be solved in principle from any initial assumption of impurity levels, provided the photon fluxes of the main constituents (*C*, *Be*, *He*) are available. The intersection of $S_{cx} = n_z n_b(0) q_{eff}^{cx} dl/dl_{cx}$ with the inverse attenuation factor $\zeta^{-1} = \exp \int n_e \sum Q_z c_z dr$ determines a unique solution. The various quantities are $Q_z(E)$ the stopping cross-section, q the effective emission coefficient, $c_z = n_z/n_e$ the impurity concentration, dl/dl the measured CX photon flux, and $n_b(0)$ the vacuum neutral beam density. For clarity the summation over the energy species has been omitted.

C. Consistency of CXRS analysis for the JET PTE pulses

A relevant test case for the self consistency of charge exchange spectroscopy analysis has been the preliminary tritium experimental (PTE) campaign of JET¹³. One of the key diagnostic issues was the data consistency required for the prediction code TRANSP in the break-up of neutron production into its thermal - thermal, beam - beam and beam- plasma fractions. A further point of interest was the levelling off of the neutron production and its abrupt termination some 300 msec later simultaneously with a massive carbon inflow. Following along the line of thoughts developed in this paper, a time and space resolved measurement of all plasma ions is crucial for both the calculation of beam deposition profiles and for the best possible assessment of deuteron densities deduced from electrons and impurities. An overview of the temporal evolution of central ion temperature, the main light impurities *C*, *Be* and *He*, the total neutron rate, and a CIII plasma boundary signal is given in fig. 8 and table 1. The impurity densities and beam stopping were

calculated in the procedure mentioned above. Assuming charge neutrality we can reconstruct from electron and impurity densities, a deuteron density profile, and together with C^{+6} ion temperature profile, a thermal-thermal neutron emission profile. A ratio of deuterium to tritium of 7:1 was used in the example of pulse #26148. fig. 9a shows a comparison of thermo nuclear neutron emissivity as deduced from CXRS measurements and the total emissivity as measured by tomographic reconstruction of a neutron profile monitor (see N.Jarvis, this conference). fig. 9b shows for a PTE reference shot (#26087) the comparison of the total thermal-thermal neutron rate deduced from the CXRS data directly and the TRANSP code predictions. Upper and lower values reflect the error bars in ion temperature and deuteron density errors due to errors in impurity densities.

The problem of carbon inflow terminating the high neutron yield pulses is still a matter of ongoing discussions at JET. In particular the mechanism causing finally a global crash following the peak neutron emission requires further investigation. It is however interesting to note that a precursor occurring approximately 300 msec prior to this event can be clearly seen from both beam emission spectroscopy and charge exchange spectroscopy signals. In view of the different cross-sections for beam stopping a carbon inflow should have, in principle, some effect on the neutral beam penetration, and there should be correlation between the reduction of emitted D_x light (fig.10) from the beam and carbon inflow (fig. 11). The radial carbon inflow is defined as

$$\Gamma_{C^{+6}}(\rho, t) = \frac{d}{dt} \int_0^\rho n_{C^{+6}}(r, t) dV(r) / A(\rho) \quad (6)$$

After a break-in of the neutral beam power at 13.1 sec, as illustrated in fig. 10,11 , an enhanced radial inflow starts at the boundary of the confined plasma ($r/a = 0.8$) and some 100 msec later in the plasma centre ($r/a = 0.2$). A turn-over is observed in the $D\alpha$ emission at $R = 3.4$ m followed later by a similar collapse at $R = 3.0$ m (plasma centre at $R = 3.1$ m, $a = 1.0$ m).

IV. SUMMARY

The paper has described the basis and practise of the atomic modelling used for the analysis of spectral data at JET, We have illustrated in several examples the successful confrontation of modelled spectral predictions, with observed spectra and the subsequent extraction of plasma data.

¹ H P Summers & M B Hooper (1983) Plasma Phys. 25, 1311.

² I G Hughes, P Briden, R Barnsley, R Giannella, H P Summers, I H Coffey & R W P McWhirter (1991) Proceedings of the Workshop on Diagnostics for Contemporary Fusion Experiments, 27 Aug.- & Sept., Villa Monasteros, Varenna, Italy, p935.

- ³ W J Dickson, P Breger, A Loarte, H Morsi, M F Stamp, & H P Summers (1991) Proceedings of the Workshop on Diagnostics for Contemporary Fusion Experiments, 27 Aug.- & Sept., Villa Monasteros, Varenna, Italy, p943.
- ⁴ K H Behringer, H P Summers, B Denne, M Forrest & M Stamp (1989) Plasma Phys. and Contr. Fusion 31, 2059.
- ⁵ A Boileau, M von Hellermann, L D Horton & H P Summers (1989) Plasma Phys. and Contr. Fusion 31, 779.
- ⁶ H P Summers, W J Dickson, A Boileau, P G Burke, B Denne-Hinnov, W Fritsch, R Giannella, N C Hawkes, M von Hellermann, W Mandl, N J Peacock, R H G Reid, M F Stamp & P R Thomas (1992) Plasma Phys. and Contr. Fusion 34, 325.
- ⁷ M von Hellermann, W Mandl, H P Summers, A Boileau, R Hoekstra, F J de Heer & J Frieling (1991) Plasma Phys. and Contr. Fusion 33, 1805.
- ⁸ M G von Hellermann, W Mandl, H P Summers, H Weisen, A Boileau, P D Morgan, H Morsi, R Konig, M F Stamp & R Wolf (1990) Rev. Sci. Instrum. 61, 3479.
- ⁹ R Konig, H P Summers, M von Hellermann, W Mandl, J Frieling, L D Horton, P Breger, H Morsi & R Wolf (1991) Proceedings of the Workshop on Diagnostics for Contemporary Fusion Experiments, 27 Aug.- & Sept., Villa Monasteros, Varenna, Italy, p925.
- ¹⁰ K-D Zastrow, H W Morsi, M Danielsson, M G von Hellermann, E Kallne, R Konig, W Mandl & H P Summers (1991) J. Appl. Phys. 70, 6732.
- ¹¹ H P Summers, P Thomas, R Giannella, M von Hellermann, W Dickson, K Lawson, W Mandl & P Briden (1991) Z. Phys. D 21, S17.
- ¹² W G F Core (1991) JET Joint Undertaking report JET-IR(91)15.
- ¹³ P H Rebut & the JET team (1992) Nucl. Fusion 32, 187.

Table 1

Results of visible and charge exchange spectroscopy of the preliminary tritium experiment at JET

<i>Signal</i>	<i>JET pulse number</i>			
	26147	26148	26095	26087
time(s)	13.12	13.21	13.7	13.4
n_i/n_d	0.13	0.13	.01	0.0
$T_i(\psi = 0)(keV)$	17.5 ± 0.6	18.8 ± 0.8	20.7 ± 1.0	18.6 ± 0.9
$T_i(\psi = 1)(keV)$	3.3 ± 0.1	5.2 ± 0.1	3.1 ± 0.1	3.9 ± 0.1
$\langle T_i \rangle_v (keV)$	6.2 ± 0.2	8.4 ± 0.3	7.0 ± 0.4	7.3 ± 0.3
$n_d/n_e(r = 0, C, Be, He)$	0.75 ± 0.05	0.76 ± 0.05	0.83 ± 0.05	0.84 ± 0.06
$n_d(r = 0, C, Be, He)(10^{19}m^{-3})$	2.30 ± 0.15	2.10 ± 0.15	4.30 ± 0.20	3.90 ± 0.18
$Z_{eff}(r = 0, C, Be, He)$	2.00 ± 0.25	2.05 ± 0.25	1.85 ± 0.27	1.80 ± 0.25
$\langle Z_{eff} \rangle (vis.Brems.vert.)$	1.90 ± 0.30	2.00 ± 0.30	1.83 ± 0.27	1.60 ± 0.24
$\langle Z_{eff} \rangle (vis.Brems.horz.)$	2.40 ± 0.35	2.40 ± 0.36	2.12 ± 0.33	1.77 ± 0.25
$\langle Z_{eff} \rangle (C, Be, He)$	2.15 ± 0.25	2.00 ± 0.20	1.94 ± 0.25	1.75 ± 0.25
C/Be	2.30 ± 0.40	2.40 ± 0.40	3.00 ± 0.50	2.50 ± 0.40
$C(\%)$	2.70 ± 0.40	3.00 ± 0.35	2.10 ± 0.35	1.90 ± 0.30
$Be(\%)$	1.25 ± 0.25	1.25 ± 0.25	0.70 ± 0.17	0.75 ± 0.20
$He(\%)$	1.75 ± 0.35	0.60 ± 0.25	1.20 ± 0.30	1.40 ± 0.40
$N_{tot}(C^{+6})(10^{20})$	0.90 ± 0.20	1.00 ± 0.20	1.10 ± 0.20	1.35 ± 0.25
$n_{D-D}(ther.)(10^{16}s^{-1})CX$	0.90 ± 0.10	1.10 ± 0.15	2.10 ± 0.40	2.30 ± 0.30
$n_{D-D}(ther.)(10^{16}s^{-1})TRANSP$	0.75	0.85	1.88	2.50

Fig.8. Overview of the main impurity data and neutron rate in a PTE reference pulse. The high neutron yield is terminated by an inflow of carbon as indicated by the CIII plasma boundary signal.

Fig.9. a) Calculated thermal-thermal neutron rate for PTE pulse #26148 with a n_i/n_d ratio of 0.13 using CXRS data for T_i and n_d . The total neutron rate measured by the JET neutron diagnostic (see N.Jarvis, this conference). b) Comparison of CXRS derived thermal neutron rate with TRANSP predictions. Upper and lower values present errors in n_d and T_i deduced by CXRS.

Fig.10. Beam emission signals of D-alpha for the PTE reference pulse. At the time of the final neutron crash the neutral beam penetration is drastically reduced. A precursor of the crash is possibly related to an event occurring at a dip in neutral beam power at 13.1 sec.

Fig.11. The precursor event is illustrated more clearly by the onset of an enhanced inward flow of C^{+6} occurring also at 13.1 sec. A hollow carbon profile develops as indicated by the stronger increase for the outermost radii.

Diagnostic loop

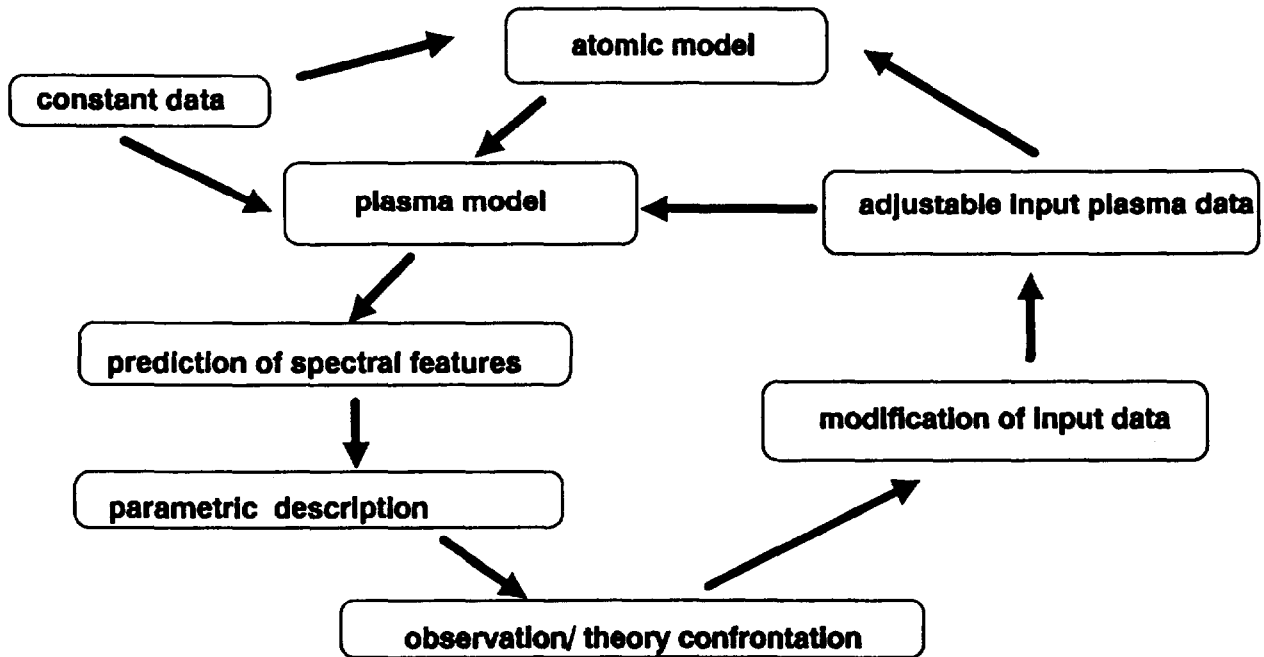


Fig.1. The 'diagnostic loop' of atomic and plasma modelling, predictions of spectral features, parametric description and finally confrontation with experimental observations. A crucial item is the extraction of physical parameters from parametrised spectra which can be cross-referenced to other diagnostics and thus an overall consistency established.

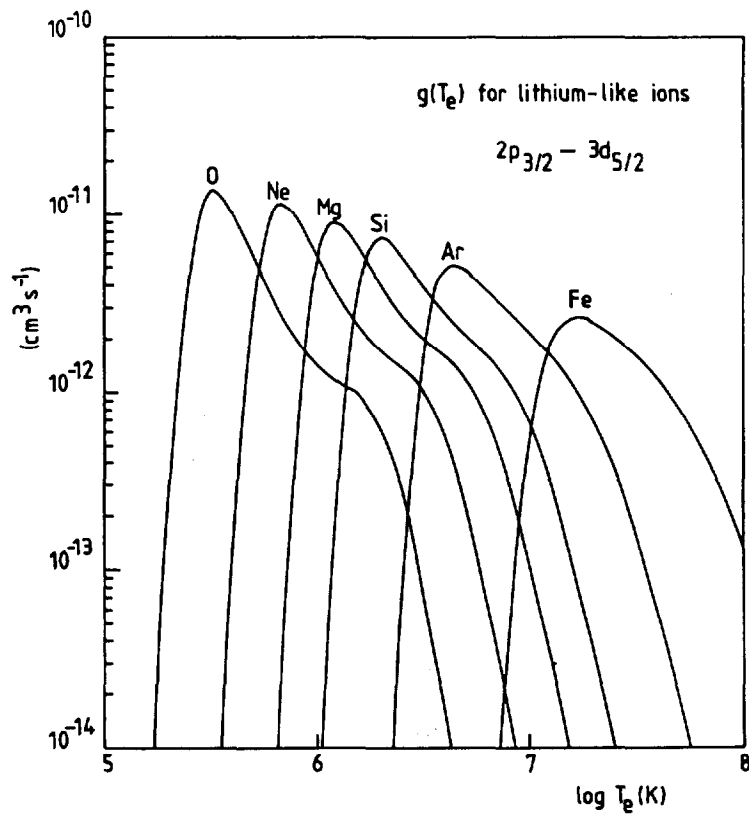


Fig.2. The $g(T_e)$ function, calculated in this example for the lithium-like ion $3d^2D_{5/2} - 2p^2P_{3/2}$ spectrum line. Note this is the constant pressure function at at $3.0 \times 10^{14} \text{ K cm}^{-3}$. For the prediction of an experimentally observed spectrum the local emissivities have to be integrated along a line of sight.

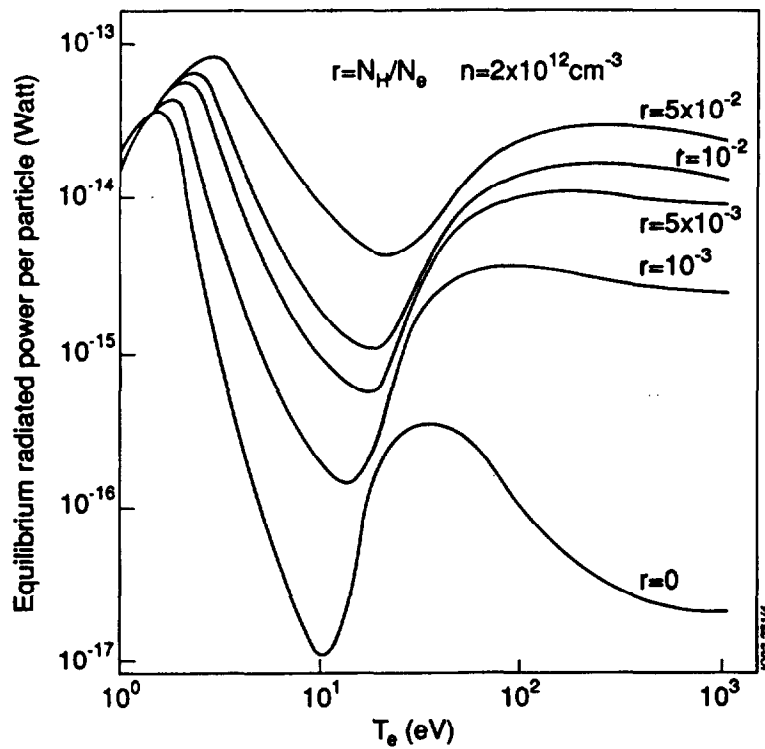


Fig.3. Effects of the neutral hydrogen to electron density ratio on the total equilibrium radiated power by beryllium.

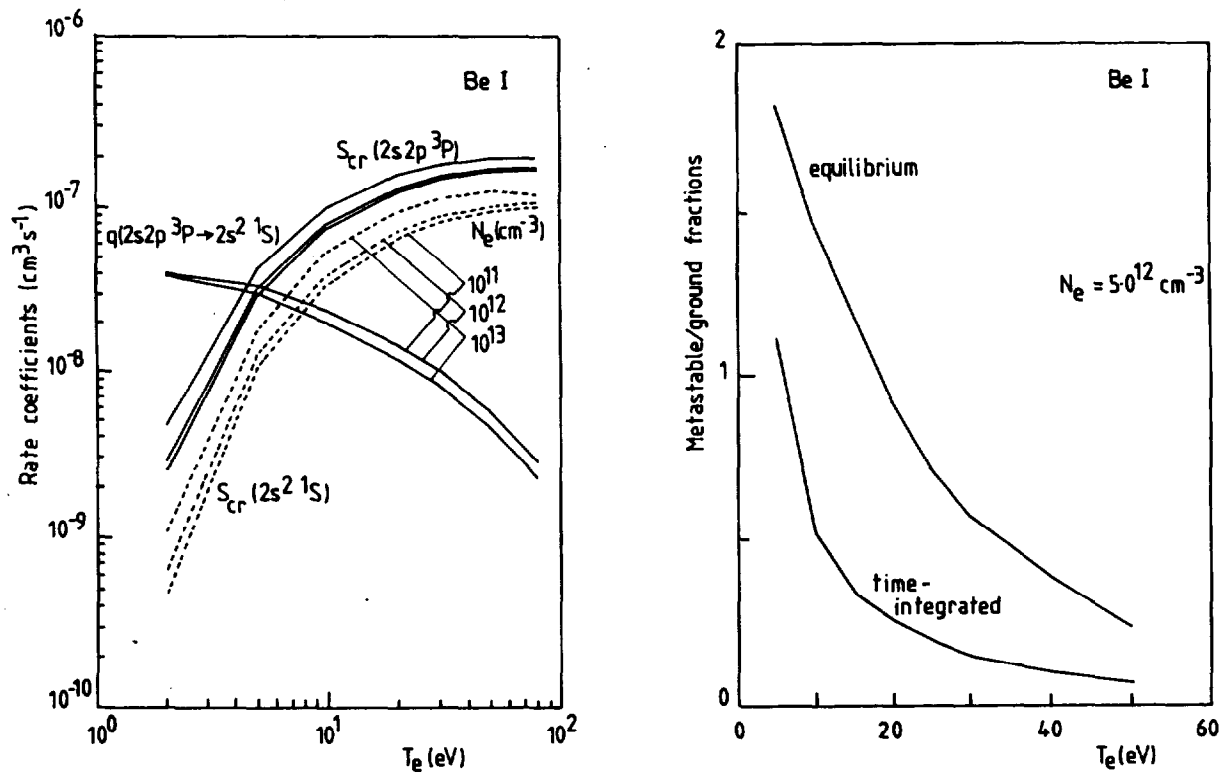


Fig.4. a) Metastable resolved collisional radiative ionisation and cross-coupling coefficients for Be^0 . Note the density dependence of the coefficients due to stepwise processes. b) Be^0 metastable/ground population fractions. The equilibrium ratio at the electron temperature is shown together with the ratio of the time-integrated populations in the fully transient model.

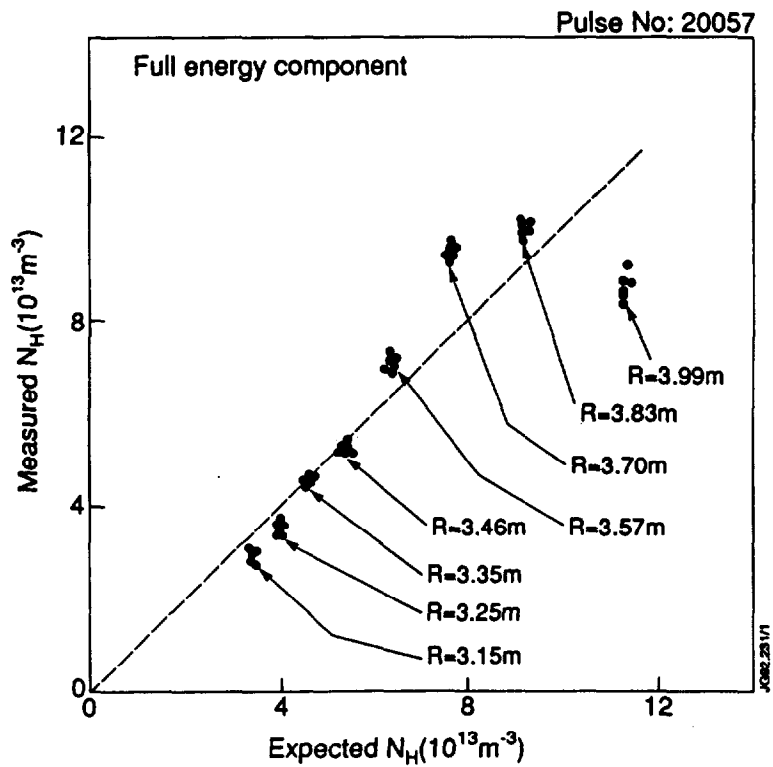


Fig.5. Neutral deuterium beam densities derived from beam emission spectroscopy of D_x and comparison to beam attenuation code calculated densities.

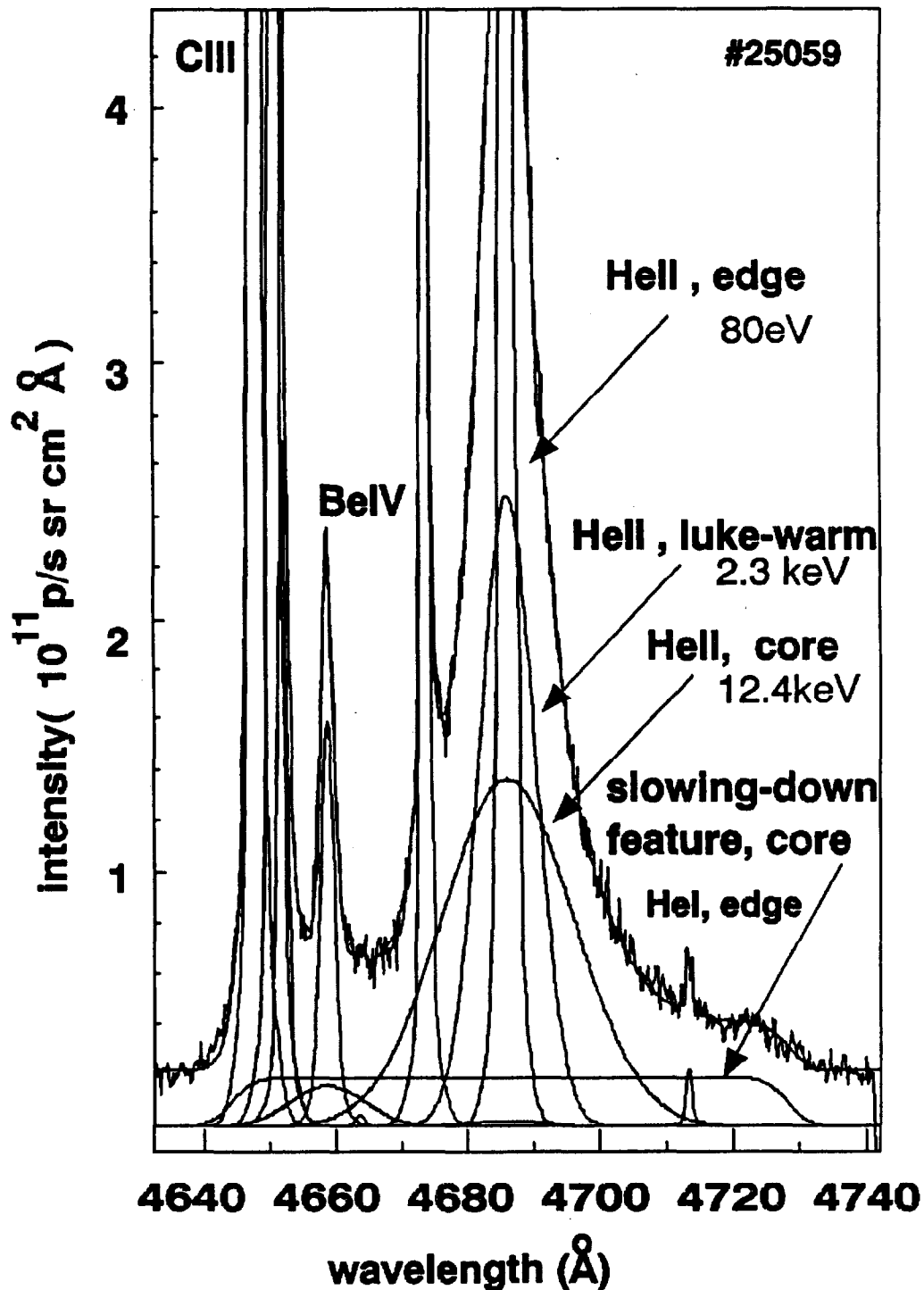


Fig.6. The multi-line spectrum for the BeIV CX lines ($n = 6-5$ at 4658.55 \AA) and ($n = 8-6$ at 4685.25 \AA) as well as the HeII CX line ($4-3$ at 4685.25 \AA). The HeII line has two 'cold' boundary features of 80eV and 2.1keV respectively. The carbon triplet at 4647 \AA is described by a $5:3:1$ line ratio. Equal temperatures are assumed for the BeIV and HeII CX features and a known emission ratio of 5.5 for $q_{\text{eff}}^2(6-5)/q_{\text{eff}}^2(8-6)$. The broad pedestal is produced by slowing-down alpha particles produced by the 135 keV neutral helium beam.

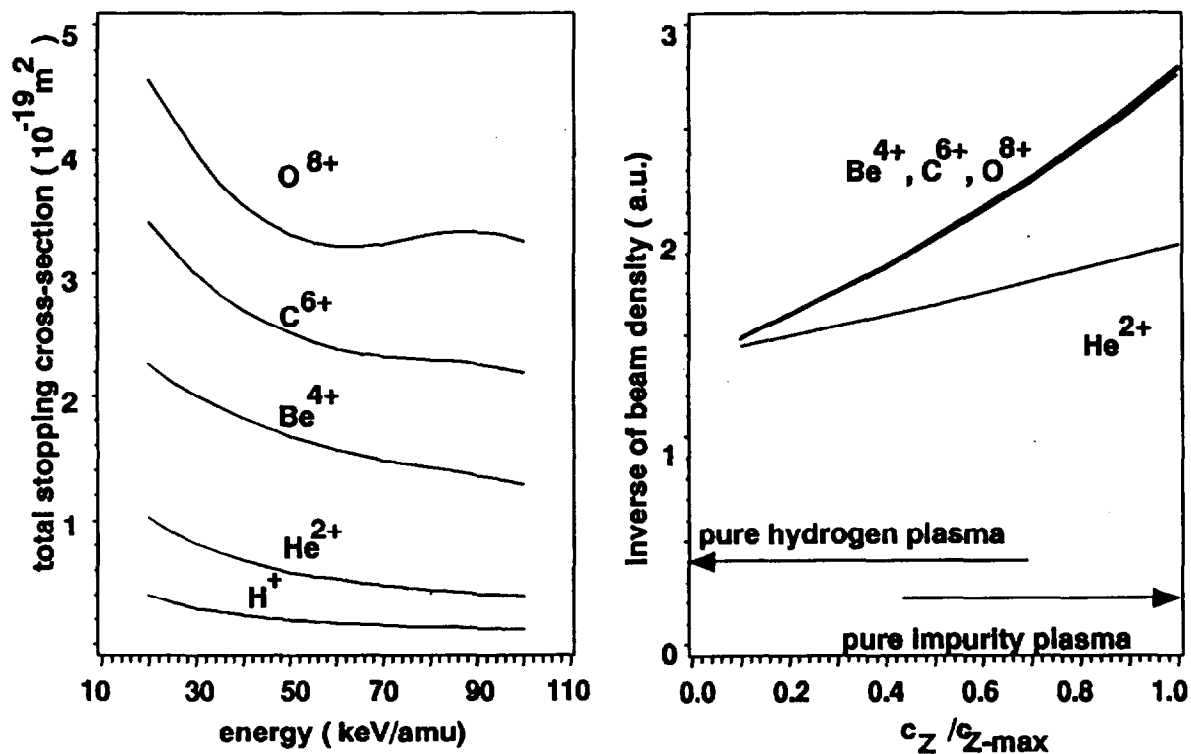


Fig.7. a) Beam stopping cross-sections for low-Z impurities for the case of a hydrogen beam. The values present the low-density case where multiple step processes are neglected. b) Inverse attenuation factor for pure hydrogen and pure impurity plasmas. In the case of carbon and beryllium the attenuation changes approximately by a factor of 2 . Beam energy is 40 keV/amu and $N_e = 3 \times 10^{19} \text{ m}^{-3}$.

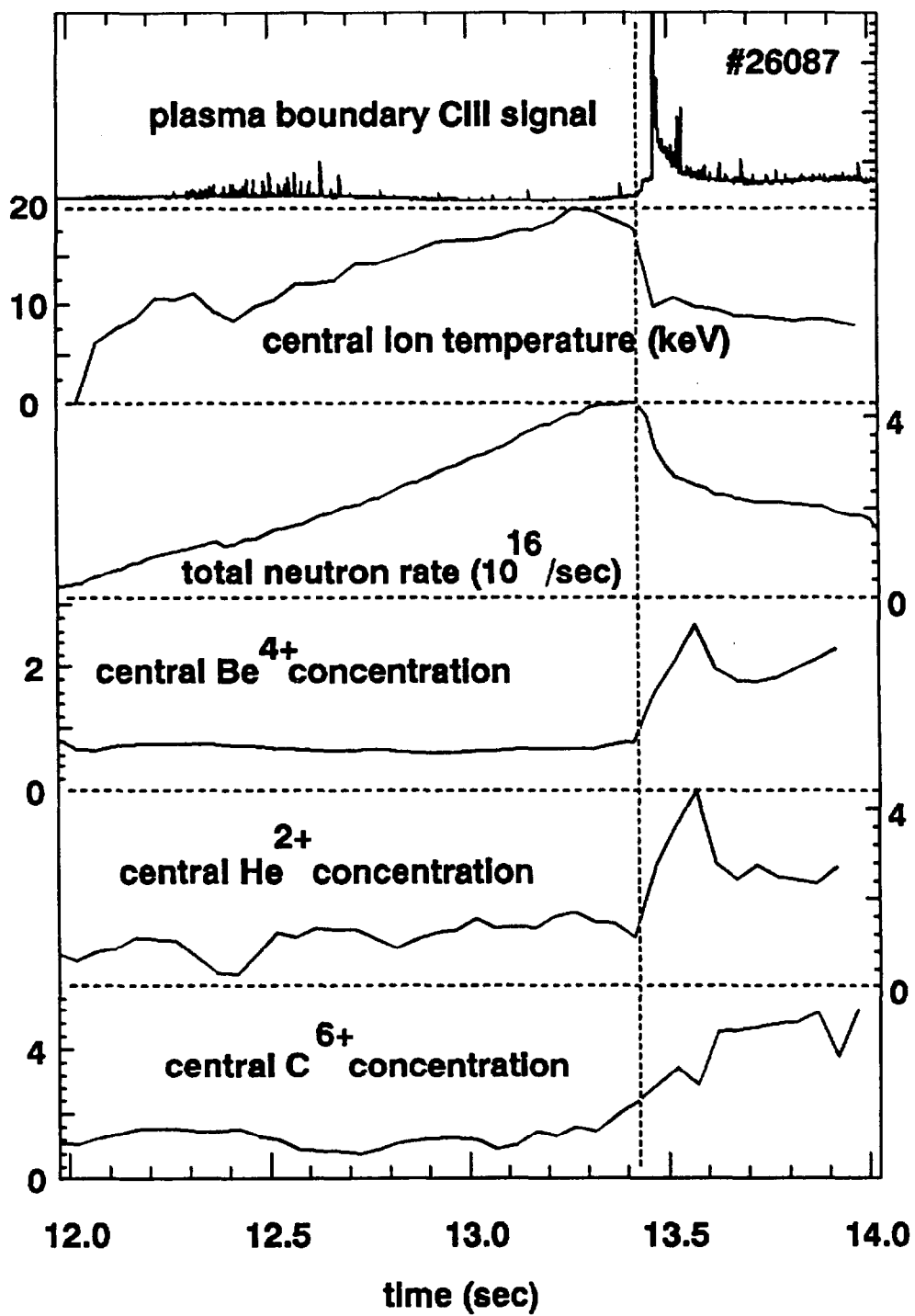


Fig.8. Overview of the main impurity data and neutron rate in a PTE reference pulse. The high neutron yield is terminated by a inflow of carbon as indicated by the CIII plasma boundary signal.

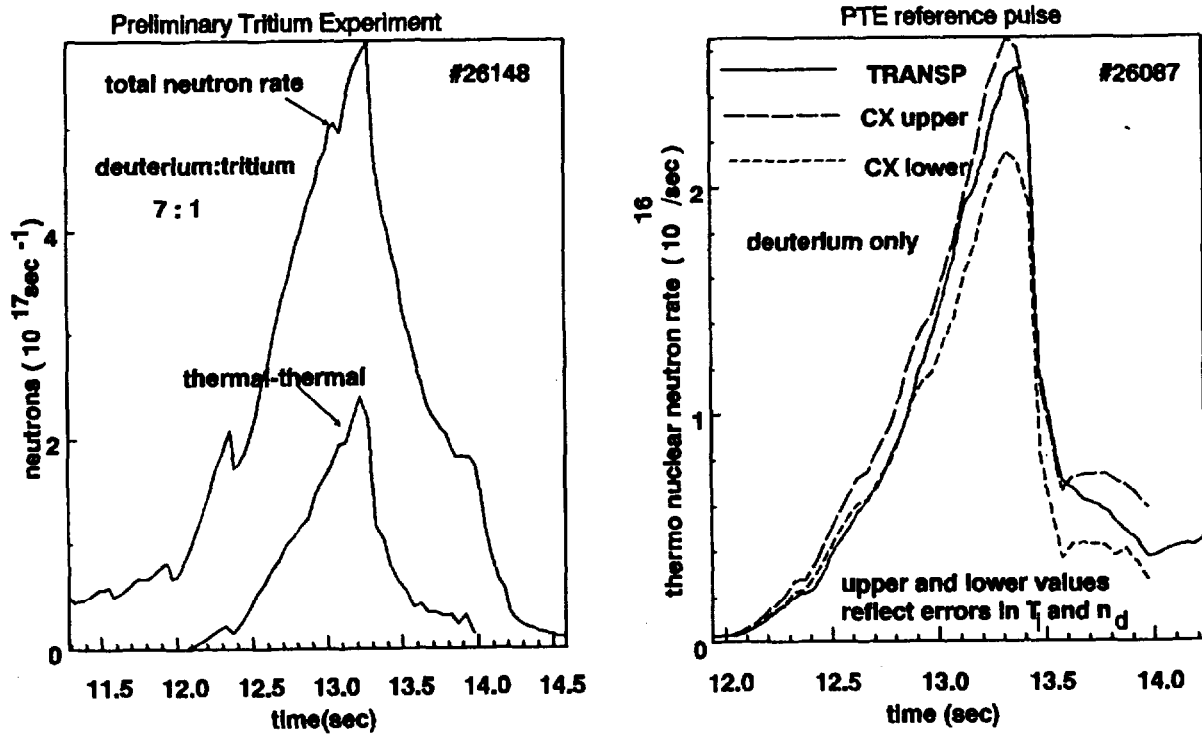


Fig.9. a) Calculated thermal-thermal neutron rate for PTE pulse #26148 with a n_i/n_d ratio of 0.13 using CXRS data for T_i and n_d . The total neutron rate measured by the JET neutron diagnostic (see N.Jarvis, this conference). b) Comparison of CXRS derived thermal neutron rate with TRANSP predictions. Upper and lower values present errors in n_d and T_i deduced by CXRS.

local Balmer-Alpha neutral beam emission intensity

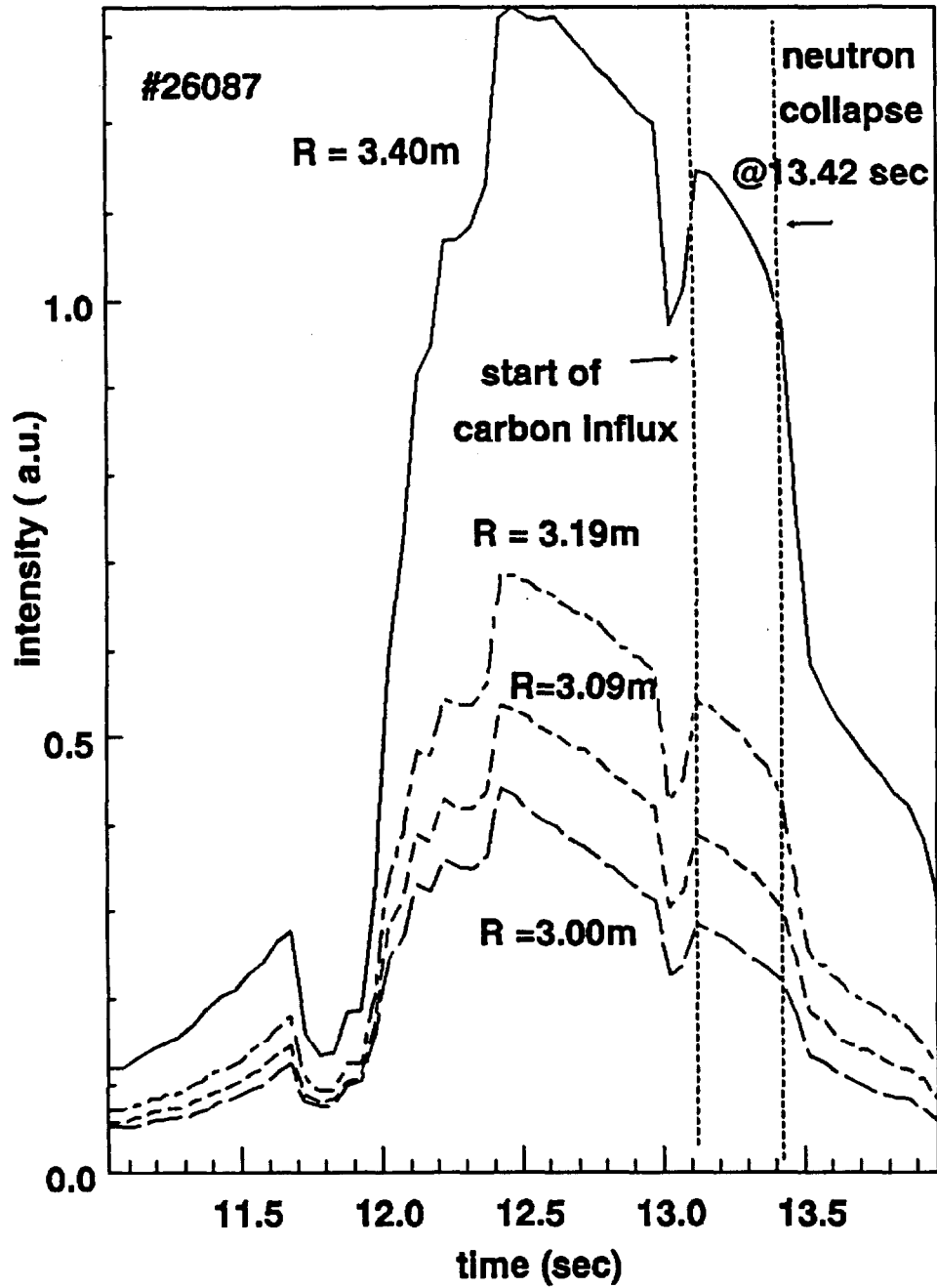


Fig.10. Beam emission signals of D-alpha for the PTE reference pulse. At the time of the final neutron crash the neutral beam penetration is drastically reduced. A precursor of the crash is possibly related to an event occurring at a dip in neutral beam power at 13.1 sec.

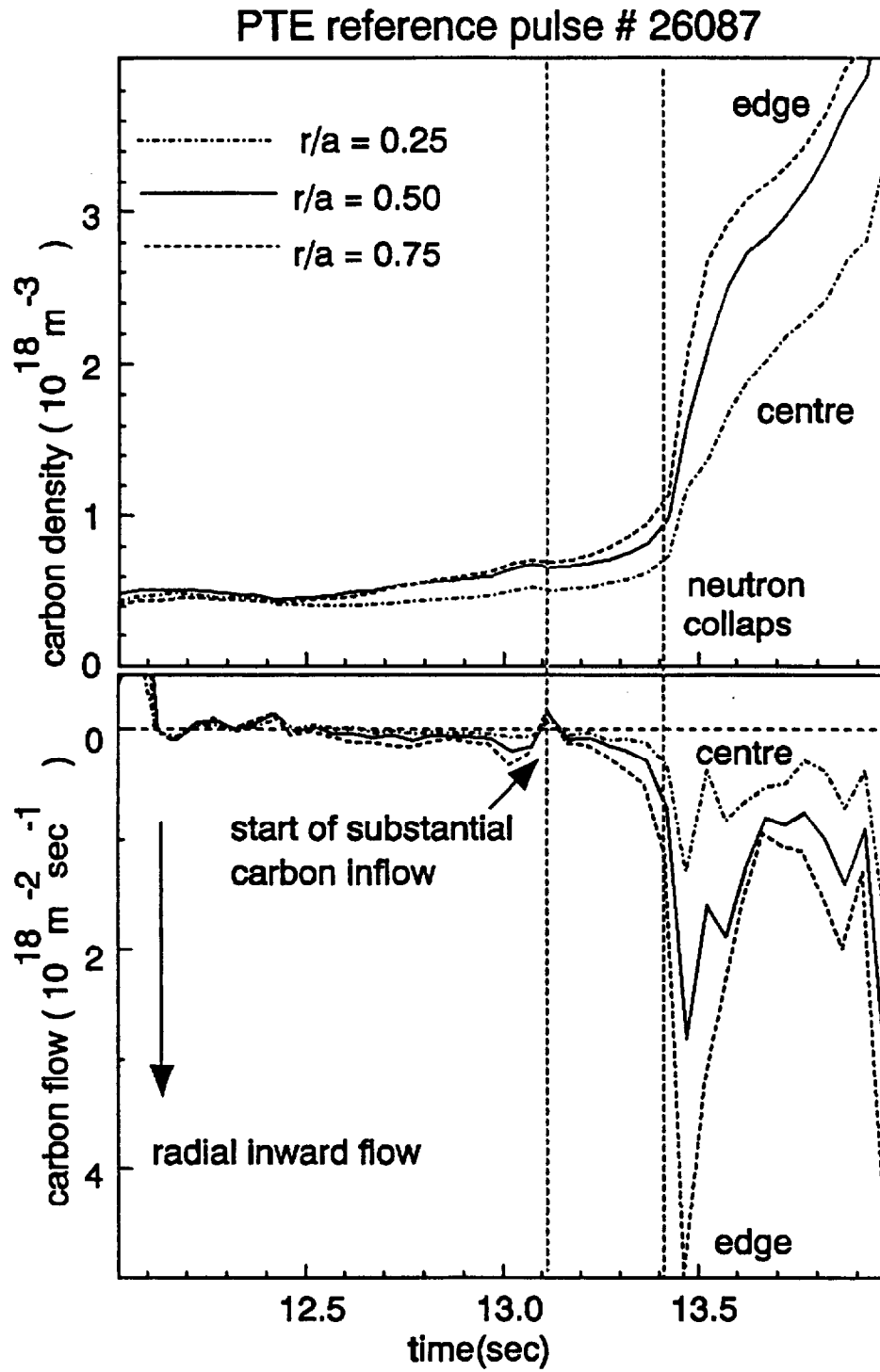
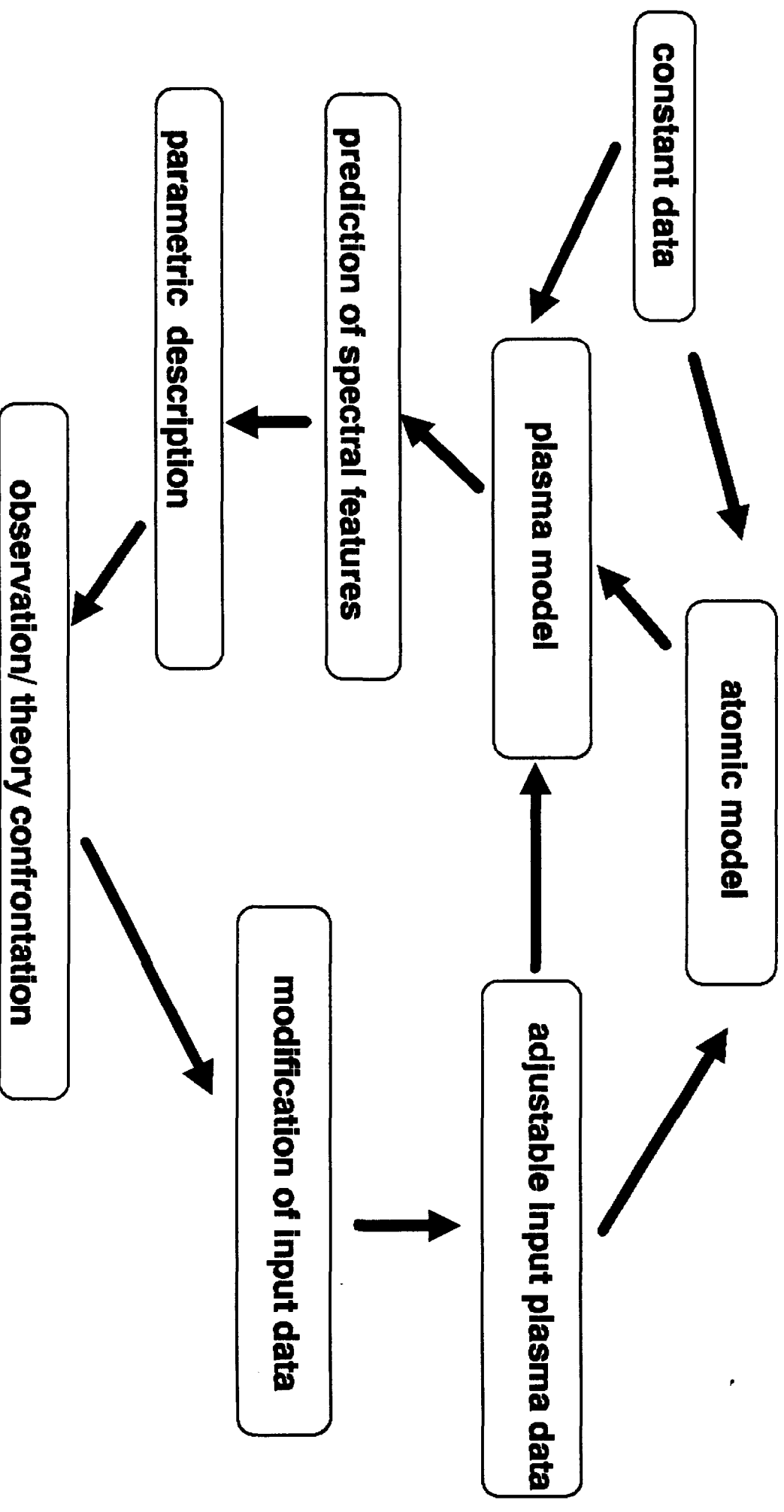
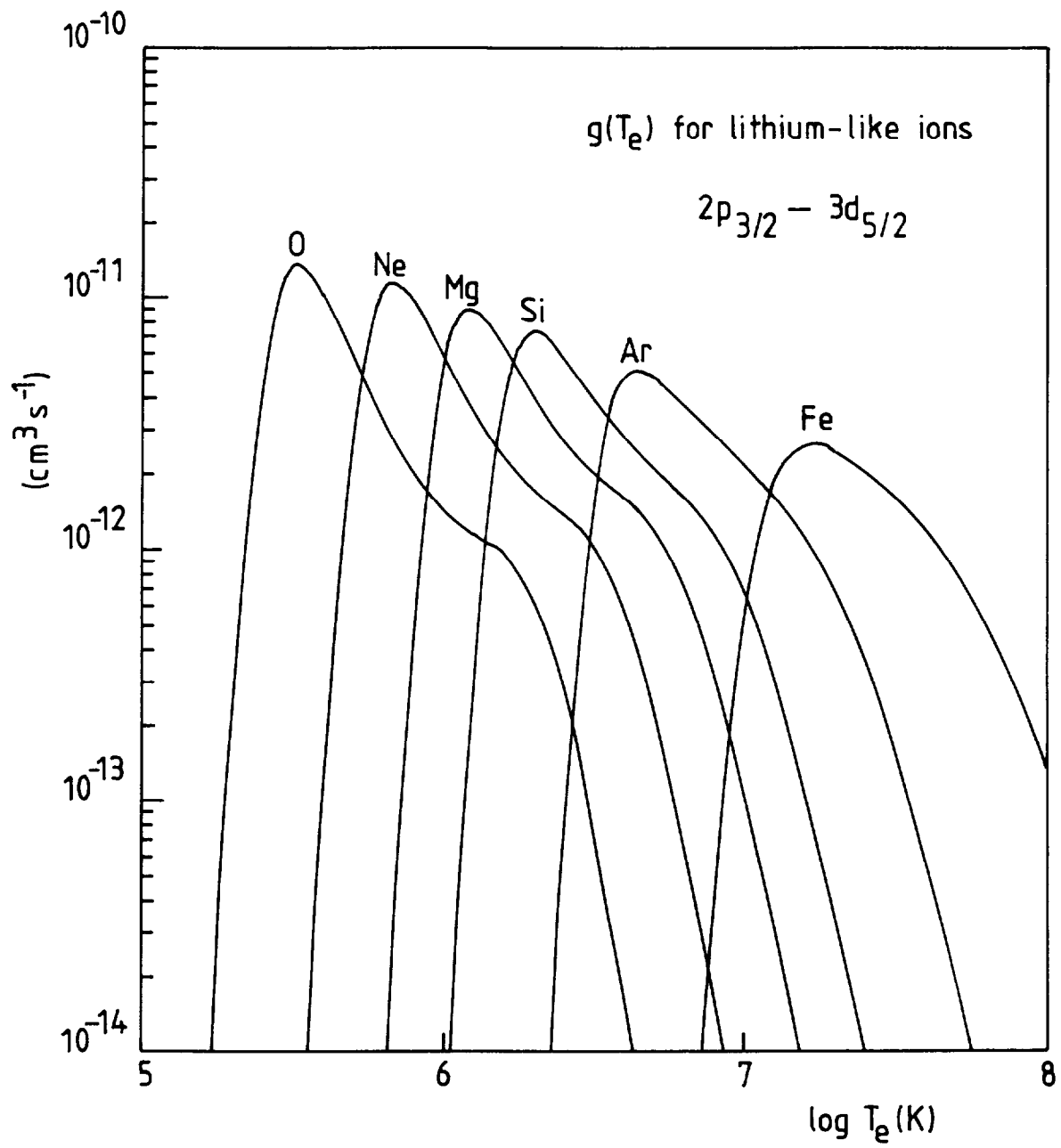


Fig.11. The precursor event is illustrated more clearly by the onset of an enhanced inward flow of C^{+6} occurring also at 13.1 sec. A hollow carbon profile develops as indicated by the stronger increase for the outermost radii.

Diagnostic loop





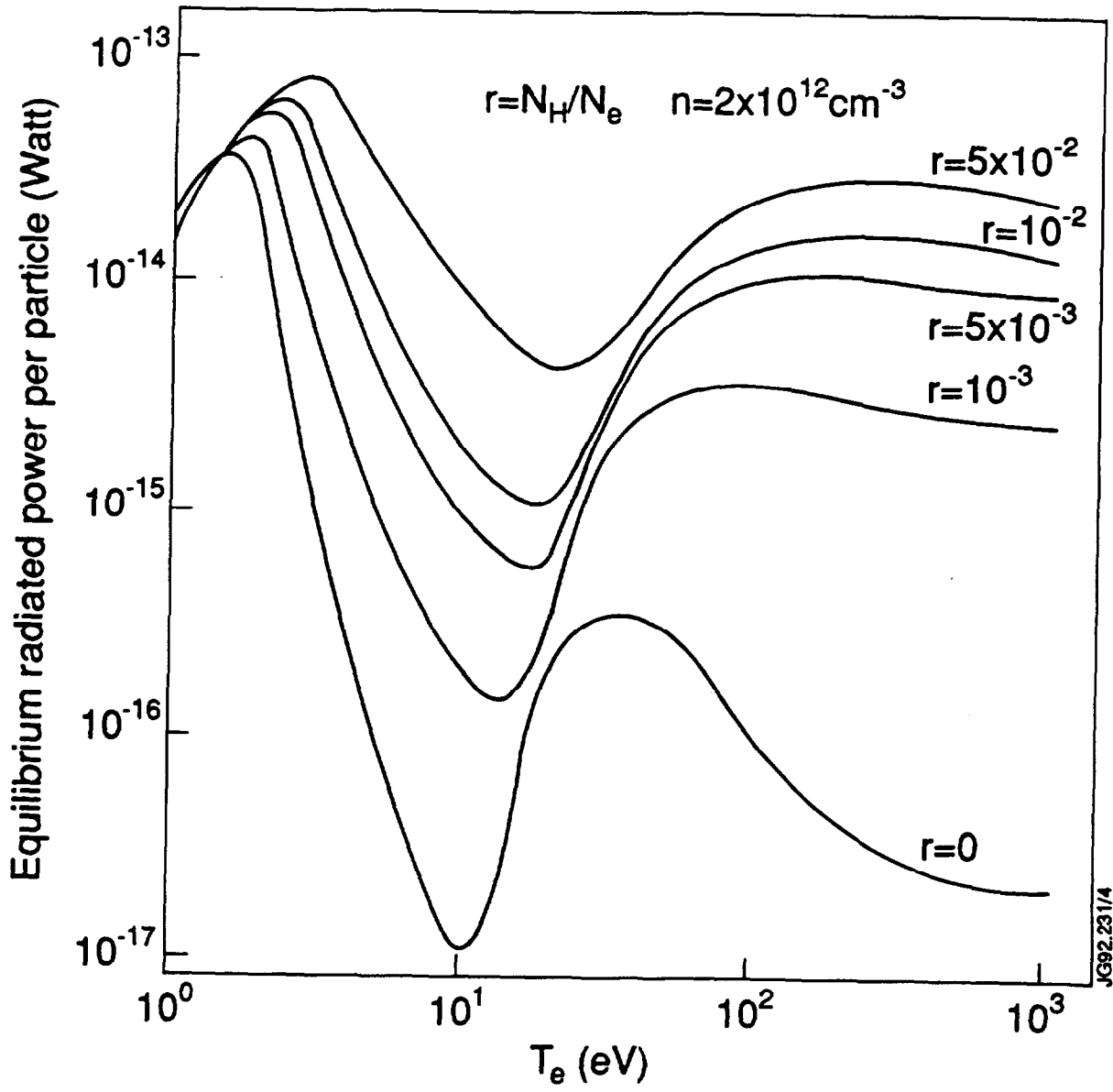
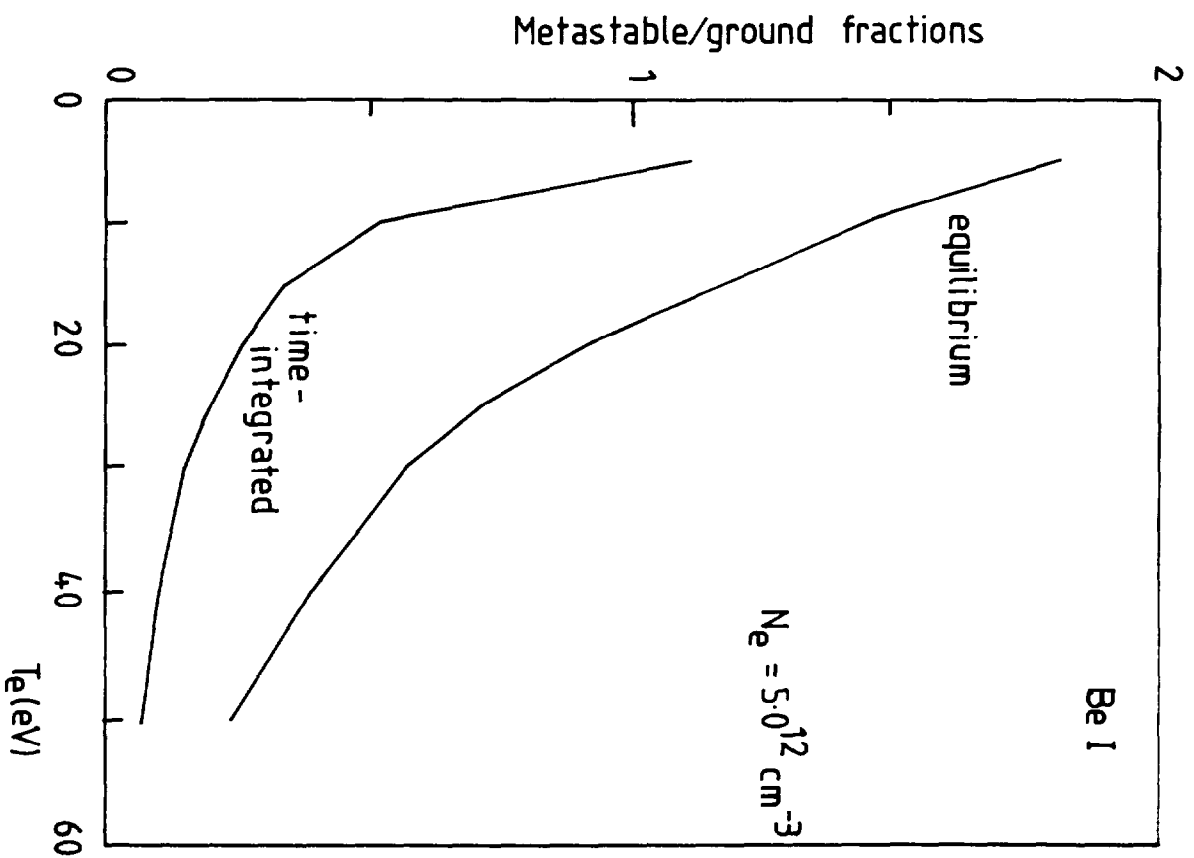
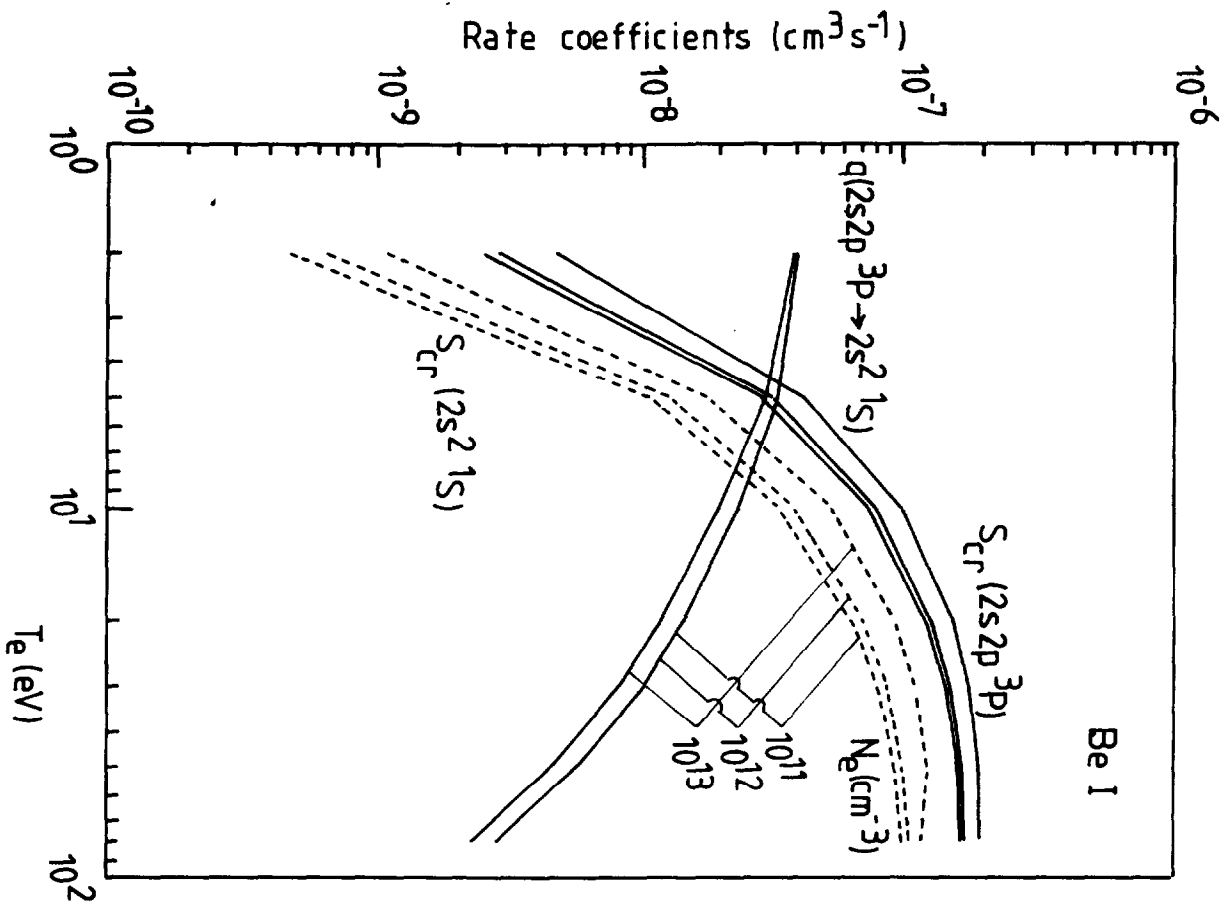
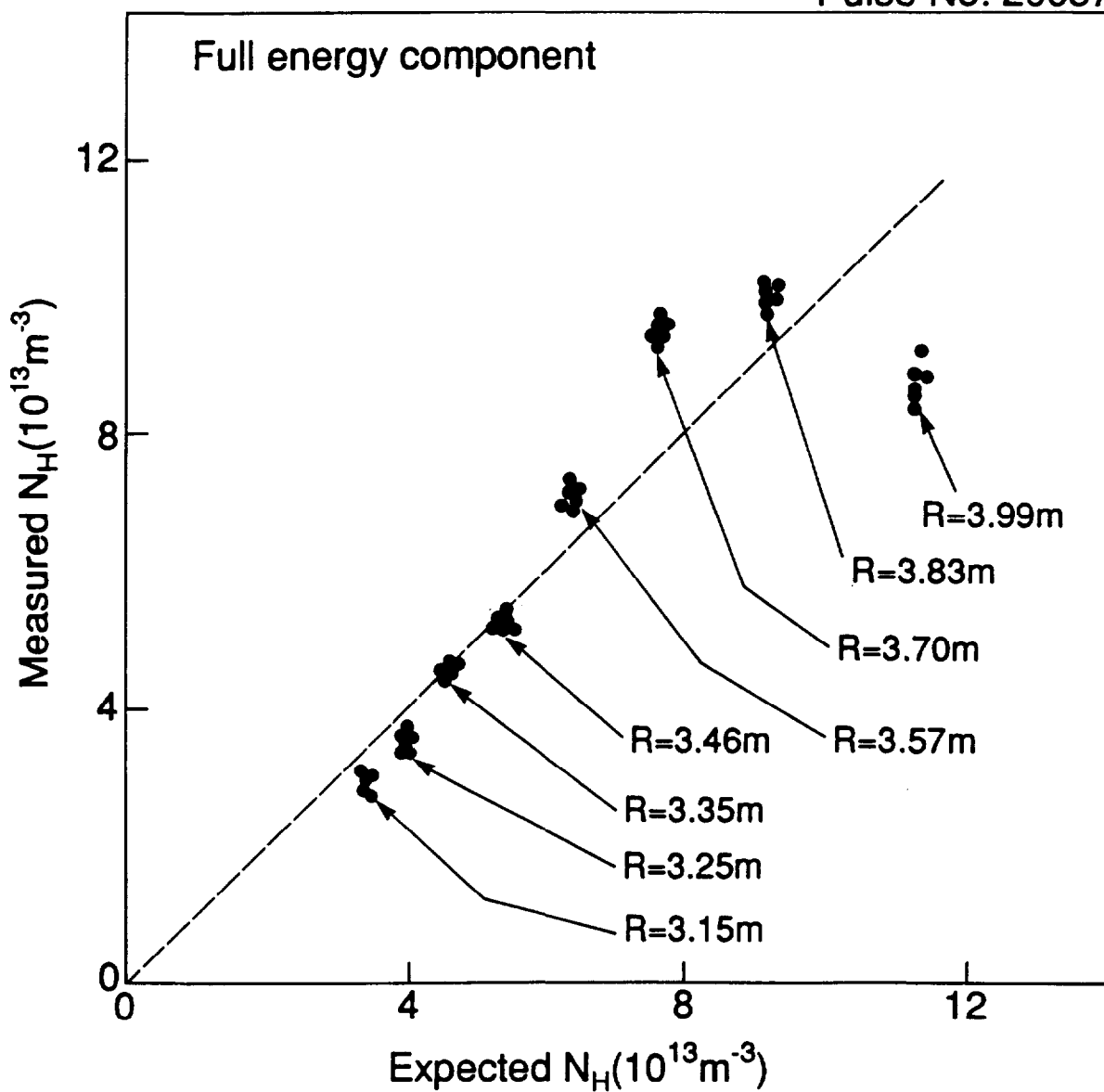


Fig 5



Pulse No: 20057



JG92.231/1

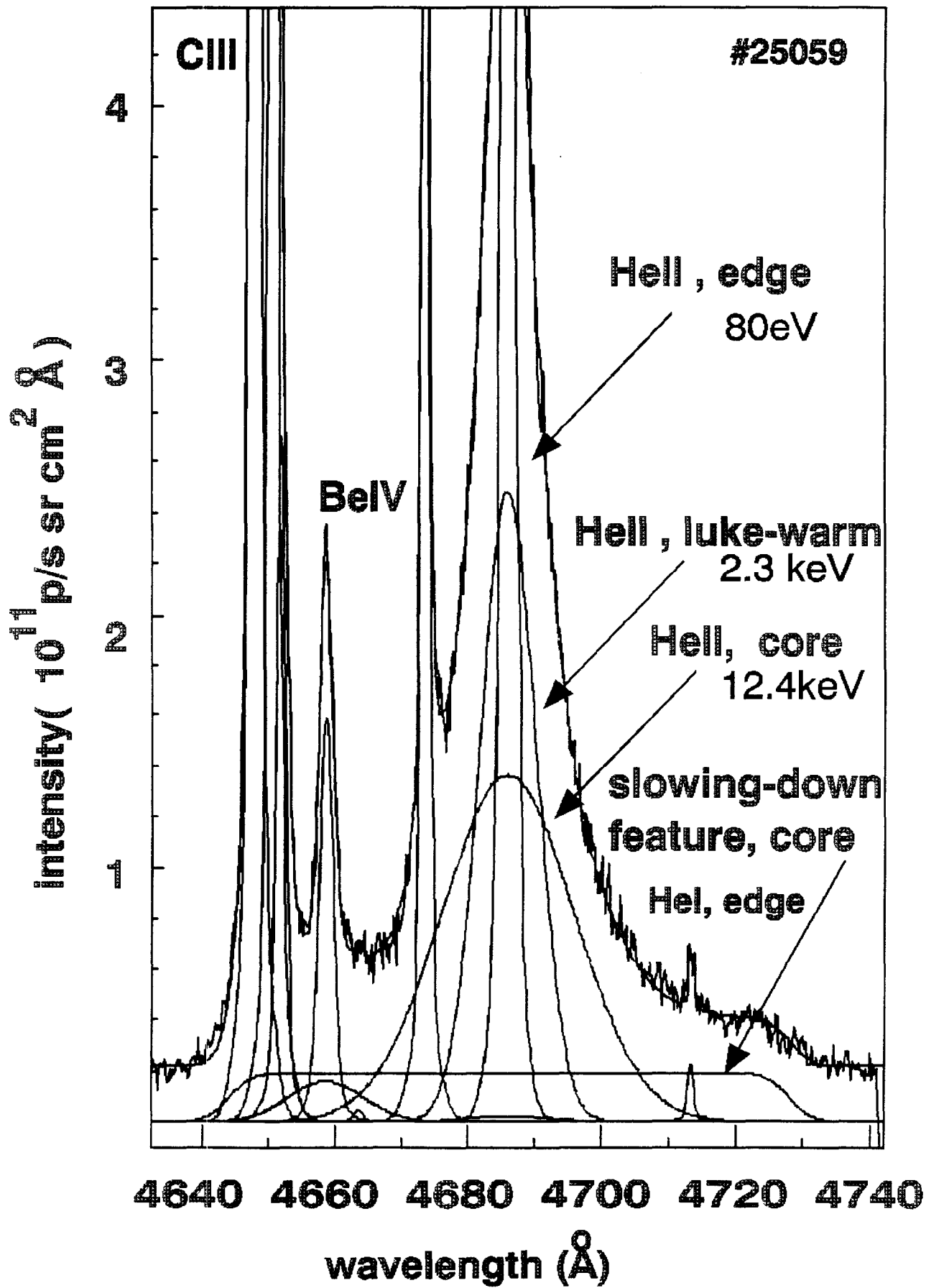
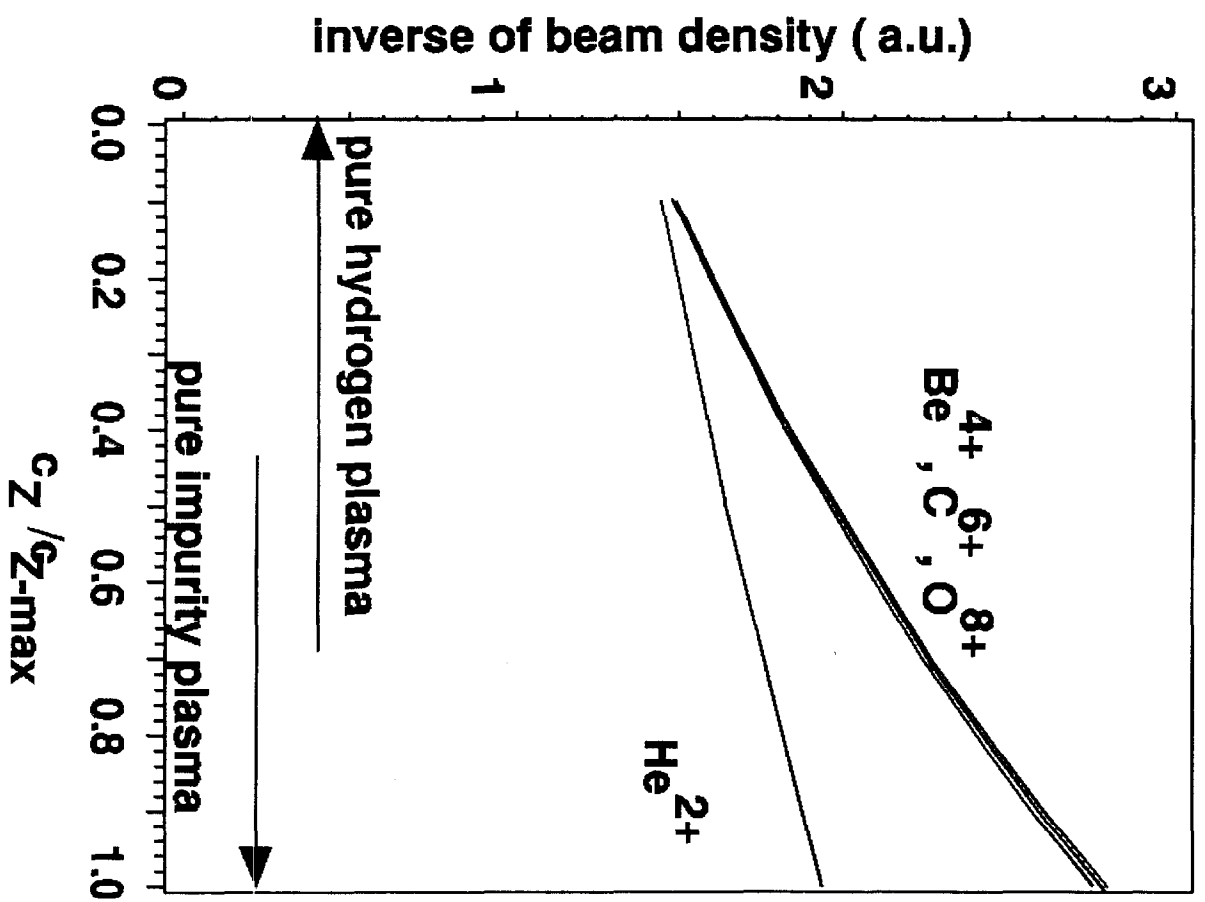
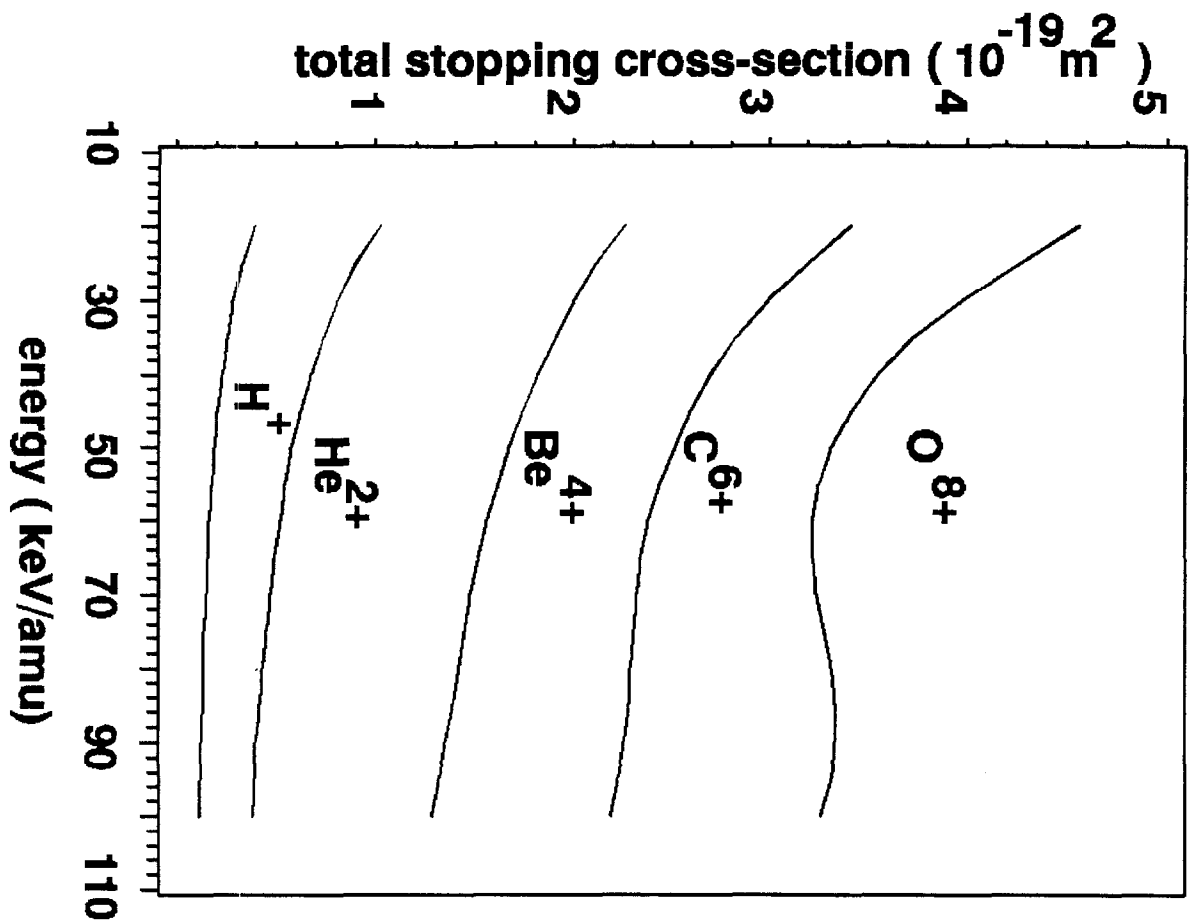
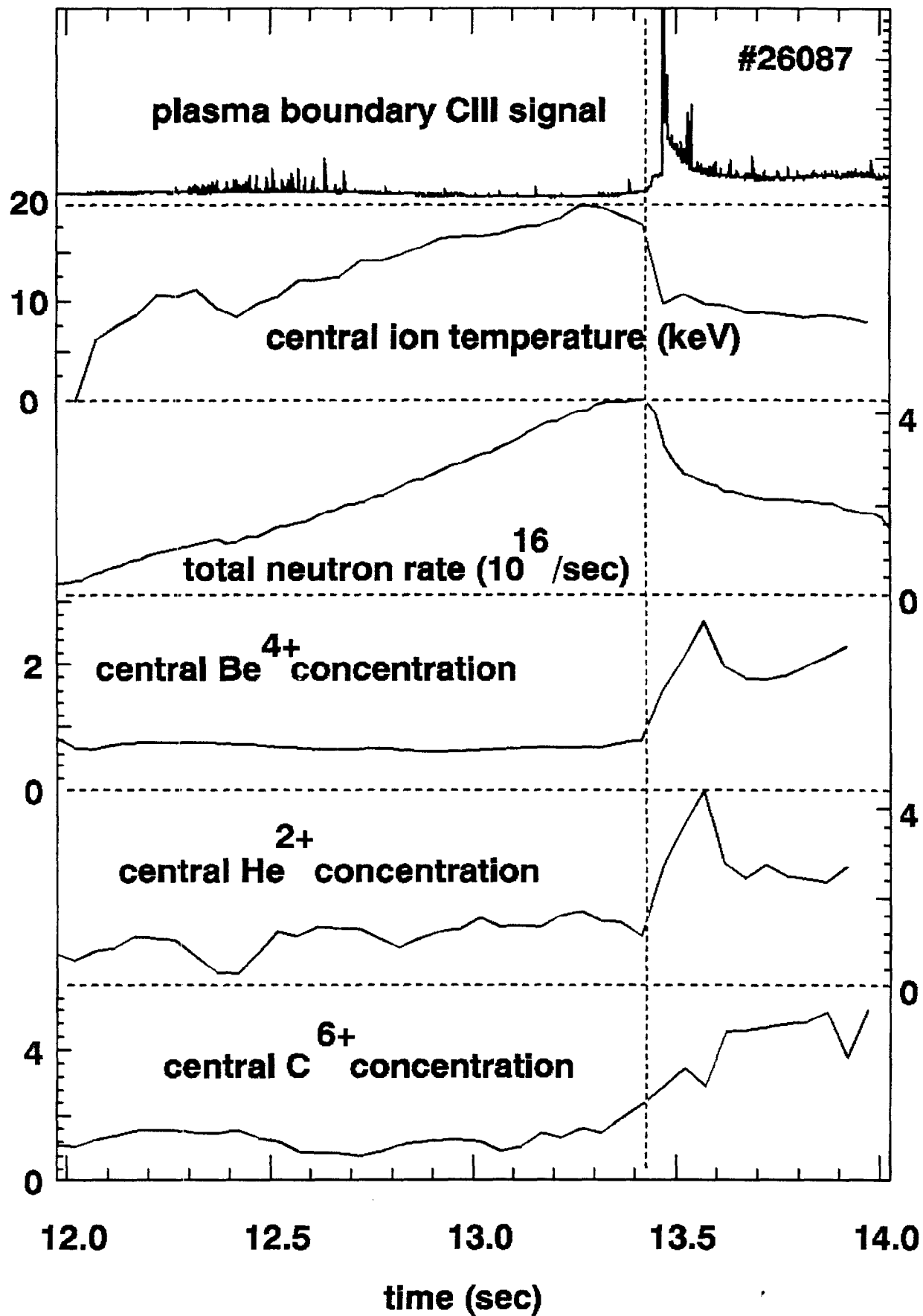
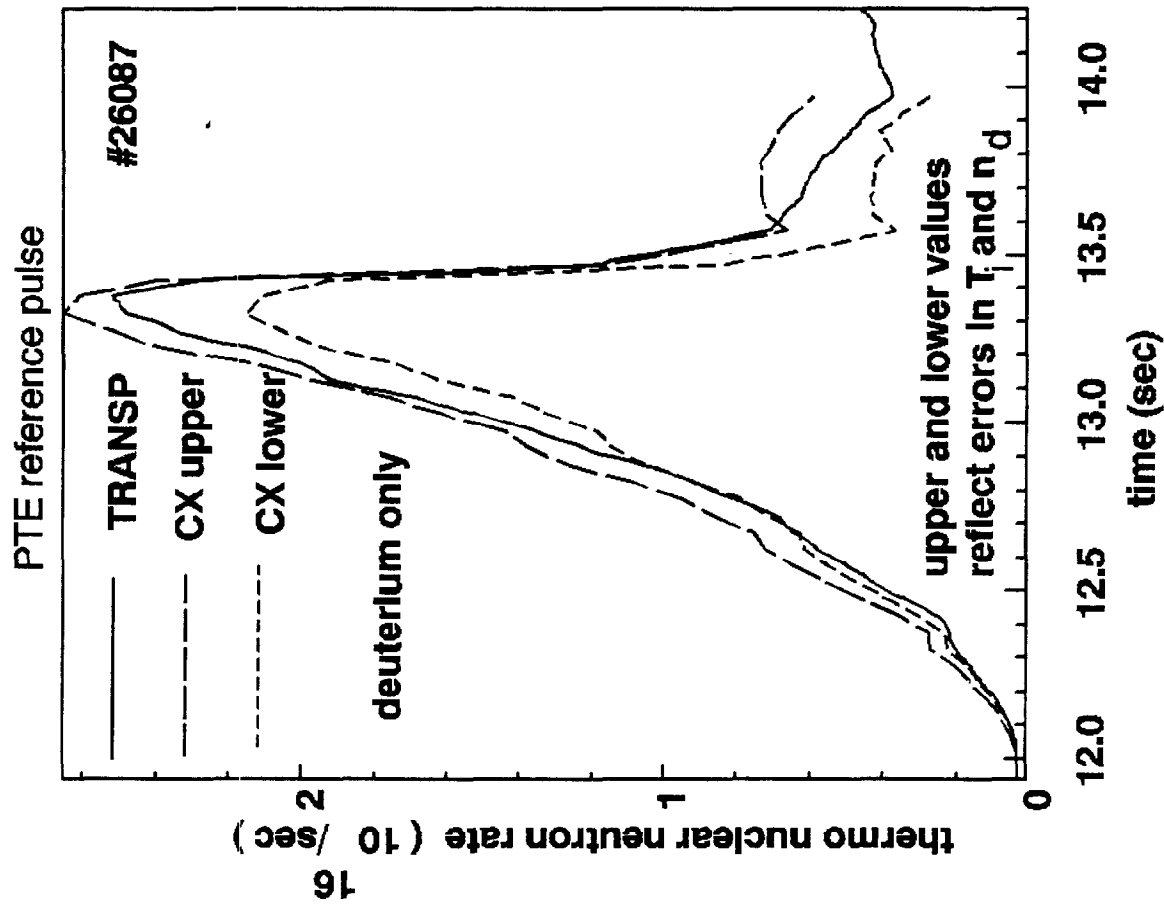
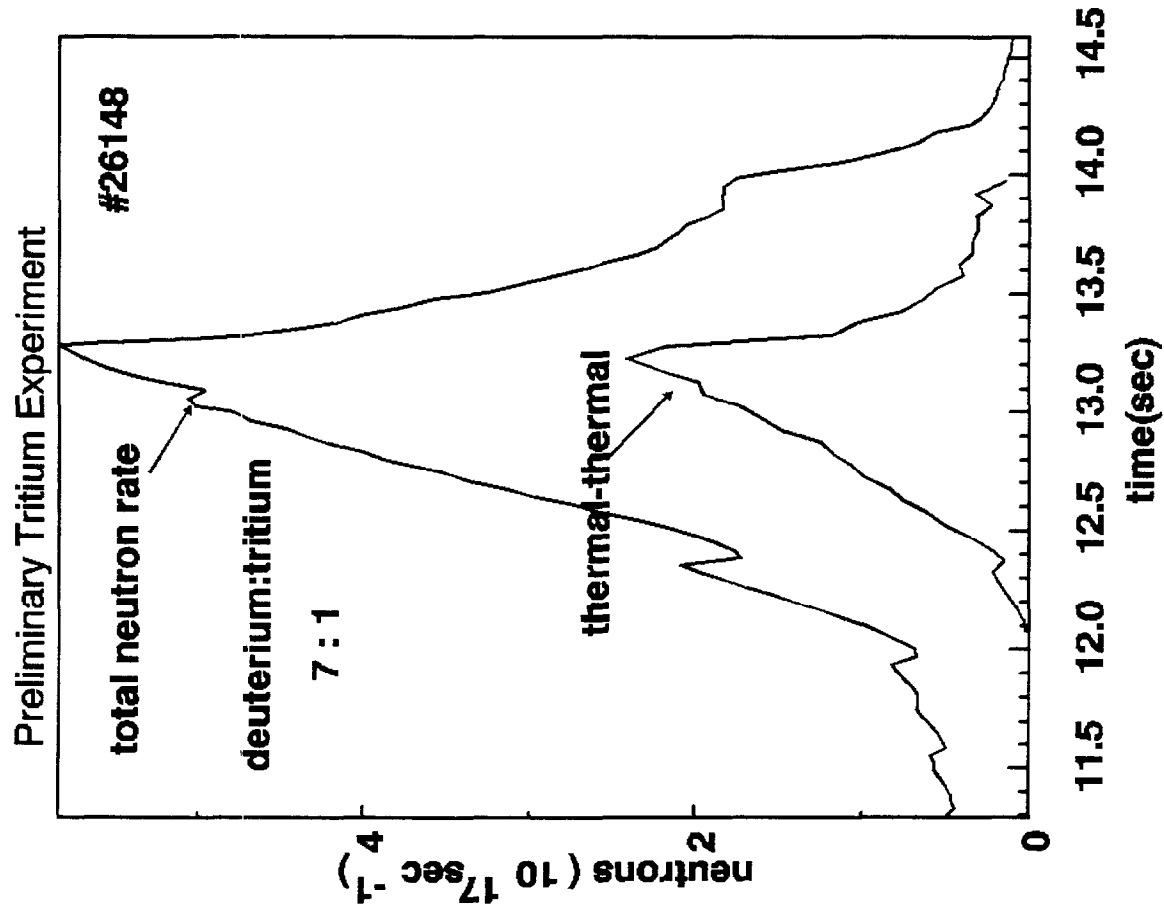


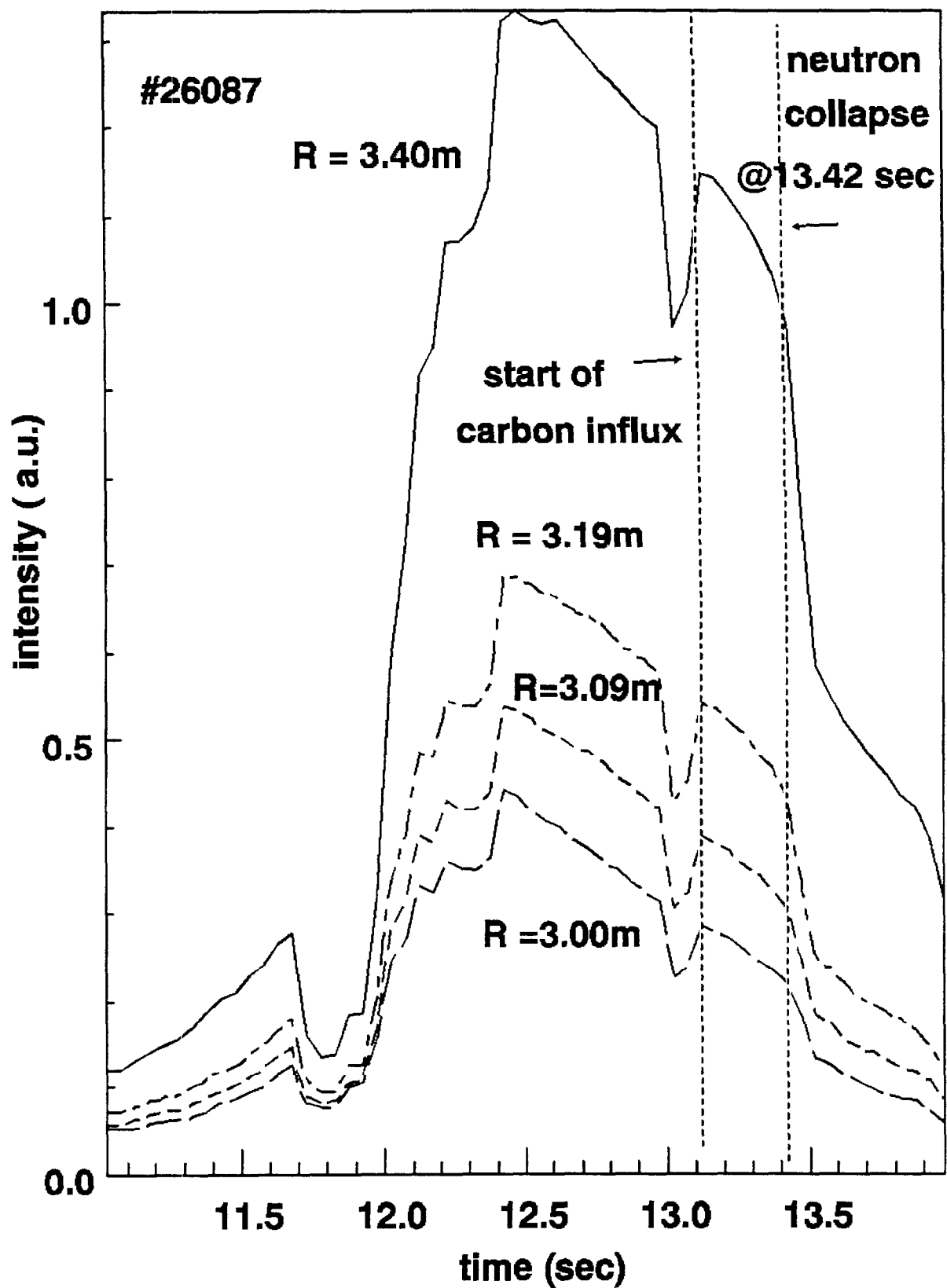
Fig 6



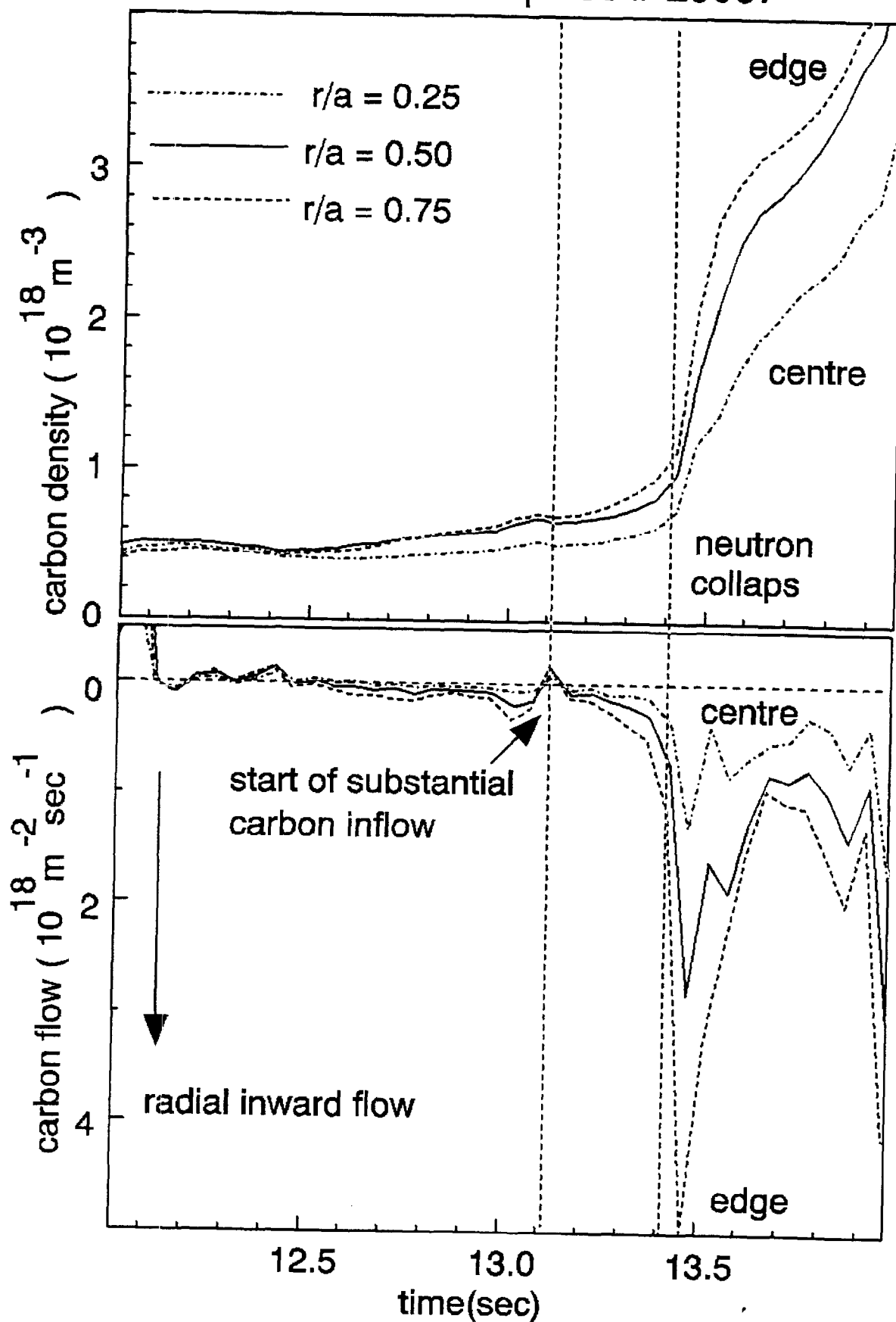




local Balmer-Alpha neutral beam emission intensity



PTE reference pulse # 26087



ANNEX

P.-H. REBUT, A. GIBSON, M. HUGUET, J.M. ADAMS¹, B. ALPER, H. ALTMANN, A. ANDERSEN², P. ANDREW³, M. ANGELONE⁴, S. ALI-ARSHAD, P. BAIGGER, W. BAILEY, B. BALET, P. BARABASCHI, P. BARKER, R. BARNESLEY⁵, M. BARONIAN, D.V. BARTLETT, L. BAYLOR⁶, A.C. BELL, G. BENALI, P. BERTOLDI, E. BERTOLINI, V. BHATNAGAR, A.J. BICKLEY, D. BINDER, H. BINDSLEV², T. BONICELLI, S.J. BOOTH, G. BOSIA, M. BOTMAN, D. BOUCHER, P. BOUCQUEY, P. BREGER, H. BRELEN, H. BRINKSCHULTE, D. BROOKS, A. BROWN, T. BROWN, M. BRUSATI, S. BRYAN, J. BRZOZOWSKI⁷, R. BUCHSE²², T. BUDD, M. BURES, T. BUSINARO, P. BUTCHER, H. BUTTGEREIT, C. CALDWELL-NICHOLS, D.J. CAMPBELL, P. CARD, G. CELENTANO, C.D. CHALLIS, A.V. CHANKIN⁸, A. CHERUBINI, D. CHIRON, J. CHRISTIANSEN, P. CHUILON, R. CLAESEN, S. CLEMENT, E. CLIPSHAM, J.P. COAD, I.H. COFFEY⁹, A. COLTON, M. COMISKEY¹⁰, S. CONROY, M. COOKE, D. COOPER, S. COOPER, J.G. CORDEY, W. CORE, G. CORRIGAN, S. CORTI, A.E. COSTLEY, G. COTTRELL, M. COX¹¹, P. CRIPWELL¹², O. Da COSTA, J. DAVIES, N. DAVIES, H. de BLANK, H. de ESCH, L. de KOCK, E. DEKSNIS, F. DELVART, G.B. DENNE-HINNOV, G. DESCHAMPS, W.J. DICKSON¹³, K.J. DIETZ, S.L. DMITRENKO, M. DMITRIEVA¹⁴, J. DOBBING, A. DOGLIO, N. DOLGETTA, S.E. DORLING, P.G. DOYLE, D.F. DÜCHS, H. DUQUENOY, A. EDWARDS, J. EHRENBERG, A. EKEDAHL, T. ELEVANT⁷, S.K. ERENTS¹¹, L.G. ERIKSSON, H. FAJEMIROKUN¹², H. FALTER, J. FREILING¹⁵, F. FREVILLE, C. FROGER, P. FROISSARD, K. FULLARD, M. GADEBERG, A. GALETSAS, T. GALLAGHER, D. GAMBIER, M. GARRIBBA, P. GAZE, R. GIANNELLA, R.D. GILL, A. GIRARD, A. GONDHALEKAR, D. GOODALL¹¹, C. GORMEZANO, N.A. GOTTARDI, C. GOWERS, B.J. GREEN, B. GRIEVSON, R. HAANGE, A. HAIGH, C.J. HANCOCK, P.J. HARBOUR, T. HARTRAMPF, N.C. HAWKES¹¹, P. HAYNES¹¹, J.L. HEMMERICH, T. HENDER¹¹, J. HOEKZEMA, D. HOLLAND, M. HONE, L. HORTON, J. HOW, M. HUART, I. HUGHES, T.P. HUGHES¹⁰, M. HUGON, Y. HUO¹⁶, K. IDA¹⁷, B. INGRAM, M. IRVING, J. JACQUINOT, H. JAECKEL, J.F. JAEGER, G. JANESCHITZ, Z. JANKOVICZ¹⁸, O.N. JARVIS, F. JENSEN, E.M. JONES, H.D. JONES, L.P.D.F. JONES, S. JONES¹⁹, T.T.C. JONES, J.-F. JUNGER, F. JUNIQUE, A. KAYE, B.E. KEEN, M. KEILHACKER, G.J. KELLY, W. KERNER, A. KHUDOLEEV²¹, R. KONIG, A. KONSTANTELLOS, M. KOVANEN²⁰, G. KRAMER¹⁵, P. KUPSCHUS, R. LÄSSER, J.R. LAST, B. LAUNDY, L. LAURO-TARONI, M. LAVEYRY, K. LAWSON¹¹, M. LENNHOLM, J. LINGERTAT²², R.N. LITUNOVSKI, A. LOARTE, R. LOBEL, P. LOMAS, M. LOUGHLIN, C. LOWRY, J. LUPO, A.C. MAAS¹⁵, J. MACHUZAK¹⁹, B. MACKLIN, G. MADDISON¹¹, C.F. MAGGI²³, G. MAGYAR, W. MANDL²², V. MARCHESE, G. MARCON, F. MARCUS, J. MART, D. MARTIN, E. MARTIN, R. MARTIN-SOLIS²⁴, P. MASSMANN, G. MATTHEWS, H. McBRYAN, G. McCRACKEN¹¹, J. McKIVITT, P. MERIGUET, P. MIELE, A. MILLER, J. MILLS, S.F. MILLS, P. MILLWARD, P. MILVERTON, E. MINARDI⁴, R. MOHANTI²⁵, P.L. MONDINO, D. MONTGOMERY²⁶, A. MONTVAI²⁷, P. MORGAN, H. MORSI, D. MUIR, G. MURPHY, R. MYRNÄS²⁸, F. NAVE²⁹, G. NEWBERT, M. NEWMAN, P. NIELSEN, P. NOLL, W. OBERT, D. O'BRIEN, J. ORCHARD, J. O'ROURKE, R. OSTROM, M. OTTAVIANI, M. PAIN, F. PAOLETTI, S. PAPASTERGIOU, W. PARSONS, D. PASINI, D. PATEL, A. PEACOCK, N. PEACOCK¹¹, R.J.M. PEARCE, D. PEARSON¹², J.F. PENG¹⁶, R. PEPE DE SILVA, G. PERINIC, C. PERRY, M. PETROV²¹, M.A. PICK, J. PLANCOULAIN, J.-P. POFFÉ, R. PÖHLCHEN, F. PORCELLI, L. PORTE¹³, R. PRENTICE, S. PUPPIN, S. PUTVINSKII⁸, G. RADFORD³⁰, T. RAIMONDI, M.C. RAMOS DE ANDRADE, R. REICHLER, J. REID, S. RICHARDS, E. RIGHI, F. RIMINI, D. ROBINSON¹¹, A. ROLFE, R.T. ROSS, L. ROSSI, R. RUSS, P. RUTTER, H.C. SACK, G. SADLER, G. SAIBENE, J.L. SALANAVE, G. SANAZZARO, A. SANTAGIUSTINA, R. SARTORI, C. SBORCHIA, P. SCHILD, M. SCHMID, G. SCHMIDT³¹, B. SCHUNKE, S.M. SCOTT, L. SERIO, A. SIBLEY, R. SIMONINI, A.C.C. SIPS, P. SMEULDERS, R. SMITH, R. STAGG, M. STAMP, P. STANGEBY³, R. STANKIEWICZ³², D.F. START, C.A. STEED, D. STORK, P.E. STOTT, P. STUBBERFIELD, D. SUMMERS, H. SUMMERS¹³, L. SVENSSON, J.A. TAGLE³³, M. TALBOT, A. TANGA, A. TARONI, C. TERELLA, A. TERRINGTON, A. TESINI, P.R. THOMAS, E. THOMPSON, K. THOMSEN, F. TIBONE, A. TISCORNIA, P. TREVALION, B. TUBBING, P. VAN BELLE, H. VAN DER BEKEN, G. VLASES, M. VON HELLERMANN, T. WADE, C. WALKER, R. WALTON³¹, D. WARD, M.L. WATKINS, N. WATKINS, M.J. WATSON, S. WEBER³⁴, J. WESSON, T.J. WIJNANDS, J. WILKS, D. WILSON, T. WINKEL, R. WOLF, D. WONG, C. WOODWARD, Y. WU³⁵, M. WYKES, D. YOUNG, I.D. YOUNG, L. ZANNELLI, A. ZOLFAGHARI¹⁹, W. ZWINGMANN

-
- ¹ Harwell Laboratory, UKAEA, Harwell, Didcot, Oxfordshire, UK.
 - ² Risø National Laboratory, Roskilde, Denmark.
 - ³ Institute for Aerospace Studies, University of Toronto, Downsview, Ontario, Canada.
 - ⁴ ENEA Frascati Energy Research Centre, Frascati, Rome, Italy.
 - ⁵ University of Leicester, Leicester, UK.
 - ⁶ Oak Ridge National Laboratory, Oak Ridge, TN, USA.
 - ⁷ Royal Institute of Technology, Stockholm, Sweden.
 - ⁸ I.V. Kurchatov Institute of Atomic Energy, Moscow, Russian Federation.
 - ⁹ Queens University, Belfast, UK.
 - ¹⁰ University of Essex, Colchester, UK.
 - ¹¹ Culham Laboratory, UKAEA, Abingdon, Oxfordshire, UK.
 - ¹² Imperial College of Science, Technology and Medicine, University of London, London, UK.
 - ¹³ University of Strathclyde, Glasgow, UK.
 - ¹⁴ Keldysh Institute of Applied Mathematics, Moscow, Russian Federation.
 - ¹⁵ FOM-Institute for Plasma Physics "Rijnhuizen", Nieuwegein, Netherlands.
 - ¹⁶ Institute of Plasma Physics, Academia Sinica, Hefei, Anhui Province, China.
 - ¹⁷ National Institute for Fusion Science, Nagoya, Japan.
 - ¹⁸ Soltan Institute for Nuclear Studies, Otwock/Świerk, Poland.
 - ¹⁹ Plasma Fusion Center, Massachusetts Institute of Technology, Boston, MA, USA.
 - ²⁰ Nuclear Engineering Laboratory, Lappeenranta University, Finland.
 - ²¹ A.F. Ioffe Physico-Technical Institute, St. Petersburg, Russian Federation.
 - ²² Max-Planck-Institut für Plasmaphysik, Garching, Germany.
 - ²³ Department of Physics, University of Milan, Milan, Italy.
 - ²⁴ Universidad Complutense de Madrid, Madrid, Spain.
 - ²⁵ North Carolina State University, Raleigh, NC, USA.
 - ²⁶ Dartmouth College, Hanover, NH, USA.
 - ²⁷ Central Research Institute for Physics, Budapest, Hungary.
 - ²⁸ University of Lund, Lund, Sweden.
 - ²⁹ Laboratório Nacional de Engenharia e Tecnologia Industrial, Sacavem, Portugal.
 - ³⁰ Institute of Mathematics, University of Oxford, Oxford, UK.
 - ³¹ Princeton Plasma Physics Laboratory, Princeton University, Princeton, NJ, USA.
 - ³² RCC Cyfronet, Otwock/Świerk, Poland.
 - ³³ Centro de Investigaciones Energéticas, Medioambientales y Tecnológicas, Madrid, Spain.
 - ³⁴ Freie Universität, Berlin, Germany.
 - ³⁵ Institute for Mechanics, Academia Sinica, Beijing, China.